Study of (in)stability of the Fourier split-step method for the massive Gross–Neveu model

T.I. Lakoba*

Department of Mathematics and Statistics, 16 Colchester Ave.,
University of Vermont, Burlington, VT 05401, USA

April 29, 2019

Abstract

We show numerically and explain analytically or semi-analytically that the well-known Fourier split-step method can exhibit three distinct types of numerical instability when used to simulate a soliton and similar solutions of the massive Gross–Neveu (also known as a nonlinear Dirac) model. To the best of our knowledge, two of the three types of this numerical instability have not previously been reported or studied in the numerical analysis literature. Moreover, these two types of instability are *unconditional*, i.e. occur for arbitrarily small values of the time step. We further show that there are two essential ingredients for observing these types of instability. One is the boundary conditions that allow a significant part of high-wavenumber radiation to remain in the computational domain over long simulation times; the common example is the periodic boundary conditions, automatically imposed by the discrete Fourier transform. The other essential ingredient is that parameter values of the soliton fall into a certain range. For the Gross–Neveu soliton this parameter is the frequency Ω. When Ω is sufficiently small, the aforementioned types of numerical instability can be sufficiently strong to be observed in simulations over moderate times. For larger values of Ω, these instabilities can still occur, but are weaker and hence could be observed only in ultra-long simulations. We also demonstrate that similar types of instabilities occur for other numerical methods applied to the Gross–Neveu soliton, as well as to some solitons of another relativistic field theory model, the Massive Thirring.

Keywords: Fourier split-step method; numerical instability; solitary waves; massive Gross–Neveu model; nonlinear Dirac equations.

---
*tlakoba@uvm.edu, 1 (802) 656-2610

1   Introduction

The split-step, or operator-splitting, method (SSM) is one of the most widely used numerical tools to model evolution of linear and nonlinear waves. It is explicit (hence straightforward to code), has a number of desirable structure-preserving properties (e.g., preserves the L_2-norm exactly in Hamiltonian systems and is symplectic), is easy to implement with the 2nd-order accuracy in time [1], and allows algorithmic extensions for higher-order accurate implementations [2–5] (see also [6] for a different approach). The idea of the SSM for wave equations is to account for linear terms with spatial derivatives, on one hand, and for all other terms, on the other hand, in separate substeps, where each of these substeps can be performed more efficiently than a step corresponding to the full evolution. A popular method to implement the substep accounting for linear terms with spatial derivatives is via (fast) discrete Fourier transform and its inverse; hence the name 'Fourier' (or 'spectral') in the corresponding version of the SSM. A vast body of literature exists on just the Fourier version of the SSM, not to mention its other (e.g., finite-difference) versions. In what follows *we will consider only the Fourier SSM and therefore will omit the modifier 'Fourier'* unless a different version of the SSM will be referred to. A (far from complete) list of application of this numerical method, focusing *only on nonlinear Hamiltonian* systems, includes: the nonlinear Schrödinger equation (NLS) [7, 8]

$$i u_t + u_{xx} + |u|^2 u = 0 \, ; \tag{1}$$

Gross–Pitaevskii equation (i.e., NLS with a potential term) with a magnetic field term [9]; Vlasov–Poisson equations [10]; nonlinear Dirac equations in one spatial dimension [11]

$$
\begin{aligned}
\psi_{1,t} + \psi_{2,x} &= i \, (|\psi_1|^2 - |\psi_2|^2 - 1)\psi_1, \\
\psi_{2,t} + \psi_{1,x} &= -i \, (|\psi_1|^2 - |\psi_2|^2 - 1)\psi_2 \, ;
\end{aligned}
\tag{2}
$$

generalized Zakharov equations [12, 13]; and Korteveg–de Vries equation [7].

Since the SSM is an explicit method, it can be only conditionally stable. Its numerical (in)stability was extensively studied for the NLS in one spatial dimension. In [14], the von Neumann analysis was applied to the SSM simulating a solution close to the plane wave, and the (in)stability threshold and the instability growth rates were found. Specifically, the instability threshold in this case is:

$$\Delta t_{\mathrm{thresh}} = \Delta x^2 \, / \, \pi, \tag{3}$$

where Δt and Δx are discretization steps in time and space. The quadratic dependence in (3) is a consequence of the "resonance", or "phase matching", condition

$$\omega \Delta t = \pi n, \qquad n \in \mathbb{N}, \tag{4a}$$

and the dispersion relation of the linear part of the NLS:

$$\omega = k^2, \tag{4b}$$

2

where ω is the frequency and $k \in [-k_{\max}, k_{\max})$ is the wavenumber;

$$k_{\max} = \pi/\Delta x. \tag{4c}$$

These results were later rediscovered, by less rigorous analyses, by researchers in fiber optical telecommunications [see, e.g., 15, 16]. Long-term behavior of the solution obtained by the SSM for the NLS with small and localized initial data was studied in [17] by the modulated Fourier expansion and in [18] by the Birkhoff normal form analysis. In [19], stability of the near-soliton (i.e., localized, not small-norm) solution was considered by a modified equation technique. While the instability threshold for the near-soliton solution is still given by (3), the instability growth rate was found to be significantly smaller than that for the plane-wave case. The same conclusions were reached, albeit only from numerical simulations, for a solution consisting of multiple pulses (as in a signal in optical communications) and a profile that varies considerably and irregularly in time [20]. In the same work, stability of the SSM for plane waves and other signals whose carrier frequency is significantly different from zero, was also considered, both by the von Neumann analysis and by numerical simulations.

Except for the NLS, we are aware of only two papers where stability of the SSM was studied systematically for nonlinear Hamiltonian systems. Namely, it was considered for the nonlinear wave (Klein–Gordon) equation in [18] and for the massive Gross–Neveu model (i.e., a Dirac equation with cubic nonlinearity in one spatial dimension) in [11]. For the nonlinear wave equation, a condition for the instability threshold was not stated explicitly, although based on the analogy with (4) above and the asymptotic (for large k) form of the linear dispersion relation,

$$\omega = \pm k, \tag{5}$$

one can conclude that it is

$$\Delta t_{\mathrm{thresh}} = \Delta x. \tag{6}$$

For the Gross–Neveu model, the stability threshold derived in [11] has the form

$$\Delta t_{\mathrm{thresh}} = O(\sqrt{\Delta x}), \tag{7}$$

which may look surprising given that the asymptotic linear dispersion relation for this model is the same as (5). Below we will demonstrate that, at least for solutions close to a solitary wave (in what follows referred to as a soliton) or multiple interacting solitons of the Gross–Neveu model, the result (7) does not hold.

Importantly for the foregoing presentation, the time step of the SSM in all previously reported studies could always be chosen small enough to render this method stable: see (3) and (6). In this work we will present, for the first time to our knowledge, examples where the SSM simulating a physically stable solution can become *unconditionally* (i.e. for an arbitrarily small Δt) unstable. More specifically, we will describe two distinct mechanisms via which unconditional, high-k numerical instability (NI) can occur when the SSM simulates a Gross–Neveu soliton.

3

Our analysis of these unconditional NI mechanisms for the Gross–Neveu solitons will be semi-numerical. That is, while we will be able to identify *how* coupling among different Fourier harmonics can drive them towards NI, and how this depends on the parameters of the soliton, the corresponding equations will turn out to be too complicated to allow analytical treatment and therefore have to be solved numerically. We believe that this semi-numerical analysis is still valuable for a number of reasons. Below in this paragraph we will name two of them, which have practical implications for situations more general than those assumed in our analysis (i.e., than for initial conditions that are infinitesimally close to the solitons of the Gross–Neveu model). Later in this Introduction we will present yet another reason. Thus, first, identifying mechanisms via which NI can occur may help recognize the same or similar mechanisms when such NI is observed in other nonlinear Hamiltonian wave equations. Second, even though the analysis necessarily assumes *stationary* (i.e., constant-shape) background solutions, its predictions about the high-k NI development remain valid for non-soliton initial conditions. We will demonstrate this by direct numerics.

In addition to analyzing unconditional NI for Gross–Neveu solitons, we will also show that there *may* also occur *conditional* high-k NI when the time step exceeds a threshold value, which turns out to be given by (6). Unlike the analysis of unconditional NI mentioned in the previous paragraph, the analysis of the conditional NI for the Gross–Neveu model will be similar to the analysis of the conditional NI of the NLS undertaken in [19]. However, that analysis for the Gross–Neveu model will yield a *qualitatively different* result from that found for the NLS. Namely, the SSM simulating an NLS soliton (or any other solution) develops a high-k NI when the time step exceeds the threshold value (3), even though the background solution is *physically* stable. In contrast, a conditional NI for the Gross–Neveu model will set in (for $\Delta t > \Delta t_{\text{thresh}} = \Delta x$) *only when the background solution is physically unstable.*

The previous sentence provides us with the opportunity to point out yet another difference in the simulations by the SSM of the solitons of the NLS, one one hand, and the Gross–Neveu model, on the other. The NLS soliton has long been known to be stable (to small perturbations of its shape); thus, any instability observed in numerical simulations is concluded to be a numerical artifact. On the contrary, stability of the Gross–Neveu soliton to infinitesimal perturbations has recently been a subject of controversy. We will present relevant details in the next section. The point that we would like to stress here is that unlike simulations for the NLS, where any instability is guaranteed to be attributable to numerical artifacts, an instability observed in simulations of the Gross–Neveu model could be of either numerical or physical nature (see Section 2). Therefore, knowing for what values of the soliton's parameters one can expect NI *and* how it can manifest itself, is useful in studies of physical (i.e., "true") stability of the Gross–Neveu soliton.

The main part of this paper is organized as follows. In Section 2 we will summarize main facts about the soliton solution of the Gross–Neveu model. In Section 3 we will present simulation results which illustrate the numerical phenomena mentioned above and thus will provide motivation for the analyses in later sections. Specifically, in Section 4 we will follow the steps of [19] and obtain a

modified equation for the high-k numerical error of the Gross–Neveu model simulated by the SSM with a time step exceeding the threshold given by (6). It will then be a straightforward matter (unlike that for the NLS [19]) to deduce that the numerical error will exponentially grow if and only if the background solution is physically unstable. Then, in Section 5, we will analyze the unconditional NI that occurs near the edges of the computational spectral window. It should be emphasized that both the analysis and the NI mechanism in this case are substantially different than those in [19]. In Section 6 we will analyze unconditional NI due to yet another mechanism, whereby *all modes* sufficiently remote from the spectral window's edges and from $k \approx 0$ (where most of the soliton's spectral content is found) are unstable in long-term simulations. In order to carry out the analyses in these two sections, we have to assume that the background solution is a single soliton, perturbed infinitesimally. In Section 7 we will demonstrate that the unconditional NIs considered in Sections 5 and 6 occur in a significantly wider variety of applications than the specific problem analyzed in those sections. Namely, we will show that these NIs can be observed when the background solution is of a more general form than a single soliton, when the SSM is applied to models similar to, but other than, the Gross–Neveu, and that they are also observed in other popular numerical methods applied to such models. We also briefly discuss how such NIs can be suppressed (although not always eliminated). In Section 8 we present conclusions of this study.

Appendices contain the following auxiliary information. Since some of our numerical results, especially those pertaining to unconditional NIs of the SSM, may appear counter-intuitive to the reader, in Appendix A we present a short Matlab code that can be used to reproduce all of the reported results for the SSM and the Gross–Neveu soliton. In Appendix B we discuss in some detail the issue of "fragility" of the Gross–Neveu soliton, introduced in Section 2. Appendices C and D contain technical results related to the analysis in Section 5. Appendices E and F contain, respectively, technical and auxiliary results related to the analysis in Section 6.

2 Soliton solution of the Gross–Neveu model and its stability

The standing soliton solution of the Gross–Neveu model (2) is [26]:

$$\{\psi_1, \ \psi_2\} \ = \ \{\Psi_1(x), \ \Psi_2(x)\} \ \exp[-i\Omega t], \qquad \Omega \in (0, 1); \tag{8a}$$

$$\Psi_1(x) \ = \ \frac{\sqrt{2(1-\Omega)} \ \cosh(\beta x)}{\cosh^2(\beta x) - \mu^2 \ \sinh^2(\beta x)}; \qquad \Psi_2(x) = i\mu \ \tanh(\beta x) \ \Psi_1(x); \tag{8b}$$

with $\beta = \sqrt{1 - \Omega^2}$ and $\mu = \sqrt{(1-\Omega)/(1+\Omega)}$. Representative members of this family for different values of Ω are shown in Fig. 1.

A soliton moving with velocity $V \in (-1, 1)$ is obtained from (8) by a Lorentz transformation (see, e.g., [27]):

$$\begin{pmatrix} \Psi_{1,\,\mathrm{mov}}(x,t) \\ \Psi_{2,\,\mathrm{mov}}(x,t) \end{pmatrix} = \frac{1}{\sqrt{2}} \begin{pmatrix} \sqrt{\Gamma+1} & \sqrt{\Gamma-1} \\ \sqrt{\Gamma-1} & \sqrt{\Gamma+1} \end{pmatrix} \begin{pmatrix} \Psi_1(x_{\mathrm{mov}}, t_{\mathrm{mov}}) \\ \Psi_2(x_{\mathrm{mov}}, t_{\mathrm{mov}}) \end{pmatrix}, \tag{9a}$$
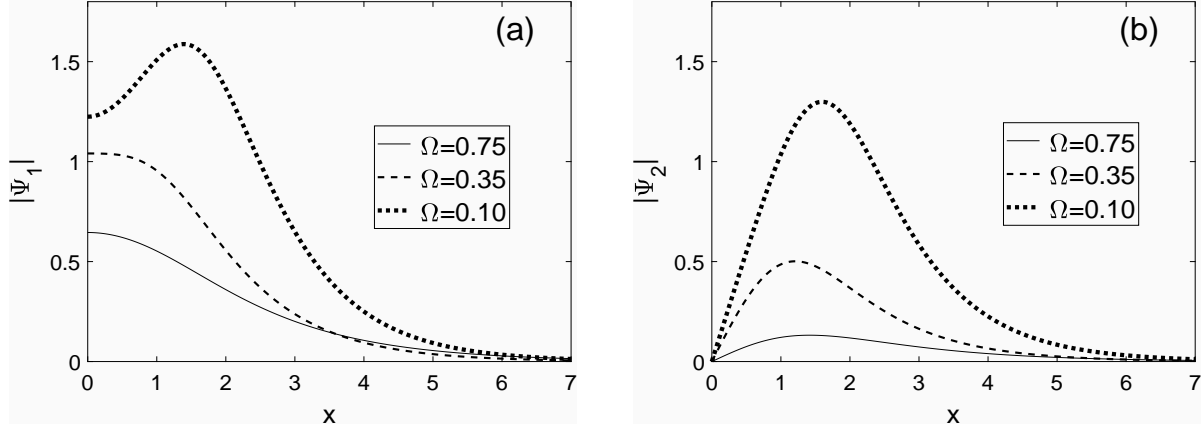
Figure 1: Components Ψ_1 (a) and Ψ_2 (b) of soliton (8). By symmetry, $\Psi_1(-x) = \Psi_1(x)$ and $\Psi_2(-x) = -\Psi_2(x)$.

where

$$\Gamma = 1/\sqrt{1 - V^2}, \qquad x_{\text{mov}} = \Gamma\left(x - x_0 - Vt\right), \quad t_{\text{mov}} = \Gamma\left(t - V(x - x_0)\right). \tag{9b}$$

For future reference we present the Gross–Neveu equations linearized on the background of the soliton (8). They are obtained by substitution of

$$\psi_{1,2} = \left(\Psi_{1,2}(x) + \widetilde{\psi}_{1,2}(x,t)\right) e^{-i\Omega t}, \qquad \left|\widetilde{\psi}_{1,2}\right| \ll 1 \tag{10}$$

into Eqs. (2) and discarding terms nonlinear in $\widetilde{\psi}_{1,2}$. Defining a vector $\widetilde{\boldsymbol{\psi}} = (\widetilde{\psi}_1, \widetilde{\psi}_2)^T$, one can write the linearized Eqs. (4) in the form:

$$\widetilde{\boldsymbol{\psi}}_t - i\Omega\,\widetilde{\boldsymbol{\psi}} + \boldsymbol{\sigma}_1\widetilde{\boldsymbol{\psi}}_x = i\,\boldsymbol{P}(x)\widetilde{\boldsymbol{\psi}} + i\,\boldsymbol{Q}(x)\widetilde{\boldsymbol{\psi}}^* \tag{11a}$$

where Pauli matrices are:

$$\boldsymbol{\sigma}_0 = \begin{pmatrix} 1 & 0 \\ 0 & 1 \end{pmatrix}, \qquad \boldsymbol{\sigma}_1 = \begin{pmatrix} 0 & 1 \\ 1 & 0 \end{pmatrix}, \qquad \boldsymbol{\sigma}_2 = \begin{pmatrix} 0 & -i \\ i & 0 \end{pmatrix}, \qquad \boldsymbol{\sigma}_3 = \begin{pmatrix} 1 & 0 \\ 0 & -1 \end{pmatrix}, \tag{11b}$$

and $\{\boldsymbol{P}, \boldsymbol{Q}\} \equiv \sum_{j=0}^{3} \boldsymbol{\sigma}_j\{P_j, Q_j\}$ with:

$$P_0 = \frac{1}{2}\left(|\Psi_1|^2 + |\Psi_2|^2\right), \qquad P_1 = 0, \qquad P_2 = \text{Im}\left(\Psi_1\Psi_2^*\right), \qquad P_3 = \frac{3}{2}\left(|\Psi_1|^2 - |\Psi_2|^2\right) - 1; \tag{11c}$$

$$Q_0 = \frac{1}{2}\left(\Psi_1^2 + \Psi_2^2\right), \qquad Q_1 = -\Psi_1\Psi_2, \qquad Q_2 = 0, \qquad Q_3 = \frac{1}{2}\left(\Psi_1^2 - \Psi_2^2\right). \tag{11d}$$

In (11c) we have used the fact that $\text{Re}(\Psi_1^*\Psi_2) = 0$. Equation (11a) can be rewritten in another form which will be convenient to refer to in what follows:

$$\begin{pmatrix} \widetilde{\boldsymbol{\psi}} \\ \widetilde{\boldsymbol{\psi}}^* \end{pmatrix}_t = \mathcal{L}\begin{pmatrix} \widetilde{\boldsymbol{\psi}} \\ \widetilde{\boldsymbol{\psi}}^* \end{pmatrix}, \qquad \mathcal{L} = \begin{pmatrix} i\boldsymbol{\sigma}_0\Omega - \boldsymbol{\sigma}_1\partial_x & 0 \\ 0 & -i\boldsymbol{\sigma}_0\Omega - \boldsymbol{\sigma}_1\partial_x \end{pmatrix} + \begin{pmatrix} i\boldsymbol{P}(x) & i\boldsymbol{Q}(x) \\ -i\boldsymbol{Q}^*(x) & -i\boldsymbol{P}^*(x) \end{pmatrix}. \tag{12}$$

Let us note that in Eqs. (11) and (12) and everywhere below, a lower-case and upper-case boldface letters indicate (2×1) vectors and (2×2) matrices, respectively.

An important issue for the study of the stability of the numerical method, which we will undertake in subsequent sections, is the *physical* (as opposed to numerical) stability of the soliton (8). To that end, we note that, on one hand, the soliton was semi-analytically proved to be linearly stable [21]. That is, all bounded eigenfunctions of the operator $\mathcal{L}$ in (12) on the infinite line were found to have only imaginary or zero eigenvalues. These results were later corroborated in [22] for two selected values of Ω: 1/3 and 2/3. On the other hand, numerical simulations by various methods detected a slow instability of an unknown origin [23, 24] for $\Omega \lesssim 0.56$ in (8). In [25] we numerically demonstrated, by a non-Fourier SSM, that the Gross–Neveu soliton is linearly stable, as predicted semi-analytically in [21], for $\Omega \geq 0.01$ (and we had no evidence to suspect that it could be unstable for smaller Ω). However, we also confirmed the observation of earlier numerical studies that for sufficiently small Ω (see below) the soliton gets increasingly (as Ω decreases) "fragile" with respect to small but finite perturbations, like those arising due to a discretization error. The origin of this empirically observed fragility is not presently understood. Nonetheless, this *physical* property of the Gross–Neveu soliton needs to be kept in mind in all numerical studies of that solution. In that regard, we will make two clarifications below.

First, we will refer to solitons that exhibit such a fragile behavior as *fragile*, as opposed to unstable. The latter term may trigger a confusion with linear instability, which would be incorrect, given that the soliton is linearly stable (see above). The term 'fragile' is, admittedly, not conventional in the mathematical literature, but it does accurately describe the empirically observed soliton's behavior. Namely, a fragile soliton may be destroyed relatively quickly by the presence of an external perturbation that is several orders of magnitude smaller than the soliton. The time that a fragile soliton can "survive" depends not as much on the size of the perturbation as on the value of Ω.

Second, it should be clarified that the aforementioned "separatrix" value $\Omega \approx 0.56$ is *not* to be regarded as a rigorous threshold between fragile and non-fragile behaviors. Rather, it is just the value *around* which a transition from one type of behavior to the other was numerically observed in [23, 24], and therefore the value near which one *can expect* a change in the long-term dynamics of a soliton simulated by other numerical methods, such as the SSM. This value depends on the simulation time and the length L of the computational domain: the greater the time and the smaller L, the greater Ω for which one observes a fragile behavior. For example, the solitons with $\Omega = 0.5$ and 0.8 were reported in [24] as fragile and non-fragile, respectively, for simulation times of $t \lesssim 15,000$ and $L \gtrsim 100$. However, in Appendix B we will present an indication that for significantly longer simulation times, the latter soliton also exhibits a fragile behavior. Accordingly, it may arguably be more appropriate to refer to some solitons as weakly fragile (e.g., to those with $\Omega = 0.75$) and to others as strongly fragile (e.g., to those with $\Omega = 0.2$), rather than as non-fragile and fragile. Evidently, this is just a semantical argument. Leaving it aside, below we will refer to solitons as fragile if they exhibit signs of fragile behavior (which will be pointed out as needed) for $t \lesssim 10,000$ and $L \sim 100$, and as non-fragile otherwise. As noted above, and in agreement with

our own simulations, the "boundary" between the two types of behavior lies around $\Omega \sim 0.6$; thus, solitons with $\Omega < 0.60$ and $\Omega > 0.60$ will be referred to as fragile and non-fragile, respectively.

Then, as we have pointed out in the Introduction, if numerical simulations of a soliton with $\Omega \sim 0.6$ or below reveal an instability, one needs to carefully analyze whether it is due to the physical fragility or to a NI, and this requires understanding of the NI properties.

3   Numerical examples motivating subsequent analysis

In the three subsections of this section we will provide results of numerical simulations that demonstrate three different types of behavior of the SSM applied to the Gross–Neveu soliton (8) (i.e., with zero velocity) which have not been observed for the NLS soliton. All of these results (as well as those reported in Sections 4 – 6 and Appendix B) can be verified using the code in Appendix A.

To put the first set of numerical results in context, recall that we have argued qualitatively, by analogy with the NLS, that (6) may be the NI threshold for the SSM applied to the Gross–Neveu model. We will present numerical results that show that this is not always the case.

The second type of behavior will reveal an NI that occurs near the edges of the computational spectral domain regardless of the time step. Finally, the third type will reveal an NI which occurs for *all* wavenumbers outside of the soliton's spectral support, also regardless of the time step.

In all simulations reported below we used the 2nd-order SSM, for which the evolution over one time step has the form:

$$
\left(\begin{array}{c} \psi_1 \\ \psi_2 \end{array} \right) (x, t + \Delta t) = \exp \left[i(\Delta t/2)\mathcal{D} \right] \ \exp \left[i\Delta t \mathcal{N} \right] \ \exp \left[i(\Delta t/2)\mathcal{D} \right] \left(\begin{array}{c} \psi_1 \\ \psi_2 \end{array} \right) (x, t), \qquad (13)
$$

where $\mathcal{D}$ is the spatial-derivative operator on the left-hand side (l.h.s.) of (2) and $\mathcal{N}$ is the operator on the r.h.s. of that system.

3.1   There may be no linear numerical instability for $\Delta t > \Delta x$

To illustrate the statement in this subsection's title, in Fig. 2 we report outcomes of a long-term evolution of a soliton with $\Omega = 0.75$ (see Fig. 1). Such a soliton has long been known to be non-fragile (see the end of Section 2). The simulation parameters are: domain length $L = 20\pi$; number of grid points $N = 2^{16}$, so that $\Delta x \approx 9.6 \cdot 10^{-4}$; and simulation time $t_{\max} = 10,000$. An explanation for using such a small Δx is found two paragraphs below. The initial condition in these simulations is taken as the soliton plus a white noise of size $\sim 10^{-12}$ in the x-domain.

Figure 2(a) confirms that when $\Delta t < \Delta x$, no trace of NI is observed. When we increase Δt to fall in the interval $(n\Delta t_{\text{thresh}}, (n+1)\Delta t_{\text{thresh}})$, where Δt_{thresh} is defined by (6) and $n \in \mathbb{N}$, we observe $2n$ spectral peaks around wavenumbers $\pm k_\pi, \ldots, \pm k_{n\pi}$, where

$$
k_{n\pi} = n\pi/\Delta t; \qquad (14)
$$

see Section 4 for a derivation. This is illustrated in Figs. 2(b)–(d). However, these peaks grow *not* exponentially in time, but either linearly or sublinearly. For example, for the parameters used in

8

obtaining Fig. 2(b), we found that peaks at $\pm k_{n\pi}$ with even n grow linearly in time, while those with odd n grow proportionally to $\sqrt{t}$: see Fig. 3(a). For different simulation parameters: Ω, L, Δx, and Δt, we have always found $k_{n\pi}$-peaks with even n grow linearly (for sufficiently long times), while those with odd n would grow either linearly or sublinearly. We do not consider these peaks in any detail below for two reasons:

(i) They do not present a case of a true, i.e. exponential, NI, since they will require an extremely long time to grow to a size where they would noticeably affect the background soliton;

(ii) We have been unable to explain the origin of these peaks.

However, we briefly list their observed properties, as well as results related to weak fragility of solitons with $\Omega > 0.6$, in Appendix B.
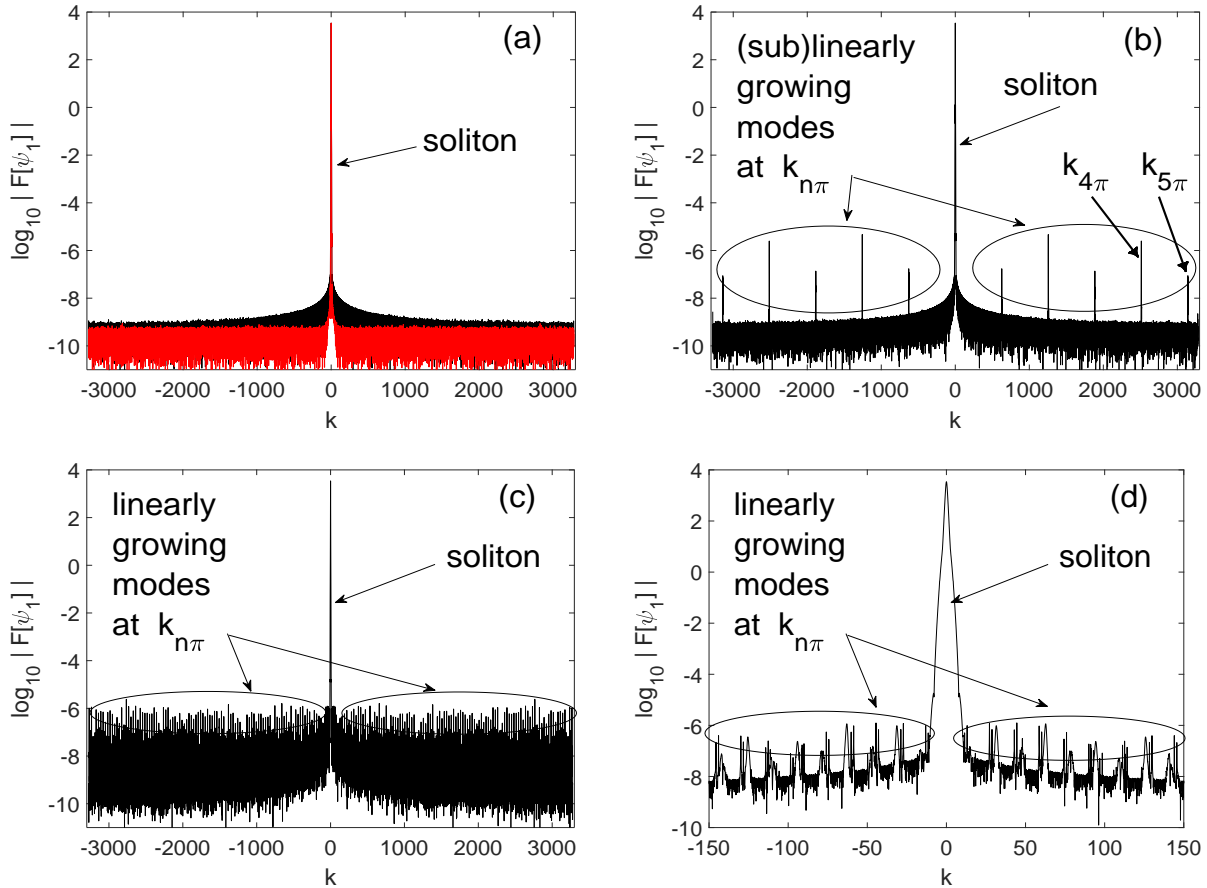

Figure 2: Numerical solution's spectrum for the initial soliton with $\Omega = 0.75$ (non-fragile). Simulation parameters are listed in the text, and: (a) $\Delta t = 0.9\Delta t_{\text{thresh}} \equiv 0.9\Delta x$; (b) $\Delta t = 0.005 \gtrsim 5\Delta t_{\text{thresh}}$; (c) $\Delta t = 0.2 \gtrsim 200\Delta t_{\text{thresh}}$. Panel (d) is a magnified view of (c), presented in order to show details of the spectrum near the soliton's spectral location. In (a)–(c) the soliton's spectrum appears as a spike because of the much wider spectral interval than in (d). In (a) only, the red curve shows the spectrum of the initial condition. In all figures in Section 3.1 we do not show results for the ψ_2-component because they are similar to those for the ψ_1-component.

In Fig. 2(c) we illustrate that the behavior of those peaks does not depend on how much Δt exceeds the "threshold" value Δx: the ratio $\Delta x/\Delta t$ affects the *number* of the peaks in agreement
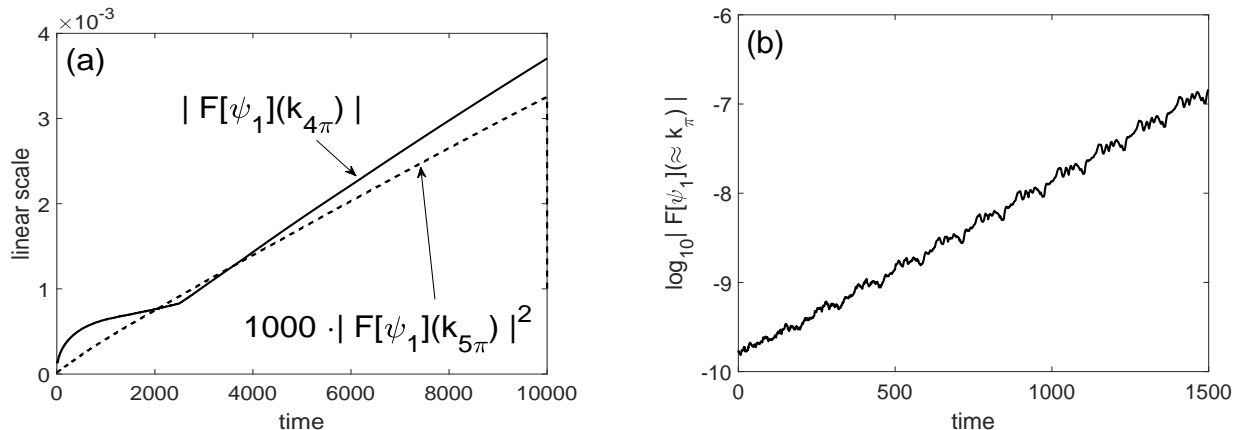
Figure 3: Evolution of the spectral components near $k_{n\pi}$. (a) Simulation parameters are as in Fig. 2(b) (non-fragile soliton). The evolution is shown for the two peaks labeled in that Figure. Note that the amplitude of the $k_{5\pi}$ peak is squared to illustrate that the original amplitude grows as $\sqrt{t}$; the empirical factor of 1000 was used only to make the two curves to be of simular magnitude. (b) Simulation parameters are as in Fig. 4(b) (fragile soliton); the amplitude of the largest mode in the group circled in that figure is shown.

with (14), but *not their growth rate*. The second purpose of Fig. 2(c) is to present evidence that the stability threshold (7), derived in [11] (see Corollary 3.5 there), is likely incorrect. Indeed, for $\Delta t = 0.2$ used to obtain Fig. 2(c), $\Delta t \approx 6.5\sqrt{\Delta x}$, and no trace of exponentially growing harmonics is seen. (It is this ability to have the ratio $\Delta t / \sqrt{\Delta x}$ to significantly exceed 1 that made us choose the Δx value to be much smaller than a value dictated by the accuracy requirement of this spectrally accurate SSM.) While the numeric constant in front of $\Delta t / \sqrt{\Delta x}$ was not specified in [11], it appears unlikely that it would exceed 1 by a greater factor than in the case reported in Fig. 2(c). Thus, the result (7) of [11] appears not to apply to the soliton of the Gross–Neveu model.

We will now show that NI *does* occur for $\Delta t > \Delta t_{\text{thresh}}$ if the background soliton is fragile. We illustrate this in Fig. 4 for the soliton with $\Omega = 0.35$ (see Fig. 1); the fragile behavior of this soliton is described in more detail in Section 3.2 below. Simulation parameters are: $L = 40\pi$ (since for a smaller Ω, $|\Psi_{1,2}(x)|$ decay slower away from $x = 0$, and we needed it to be as small as the round-off error to satisfy periodic boundary conditions); $N = 2^{12}$, so that $\Delta x \approx 0.031$ (since we no longer need to have Δx as small as in the previous case); and $t_{\max} = 1,500$. As before, white noise of the same size, $\sim 10^{-12}$, is added to the soliton in the initial condition.

In Fig. 4(a), where $\Delta t < \Delta t_{\text{thresh}}$, the resonant wavenumber k_π is outside the computational domain, and hence no NI can exist near it. The modes which appear at $k_{\max}$ (and which we verified to grow exponentially in time) occur there for *any* Δt, no matter how small, and hence are not related to the condition $\Delta t < \Delta t_{\text{thresh}}$. We will discuss them in more detail in Section 3.2. In Fig. 4(b), where $\Delta t > \Delta t_{\text{thresh}}$ and hence $k_\pi < k_{\max}$, one observes two groups of modes on both sides of k_π which grow exponentially in time: see Fig. 3(b).
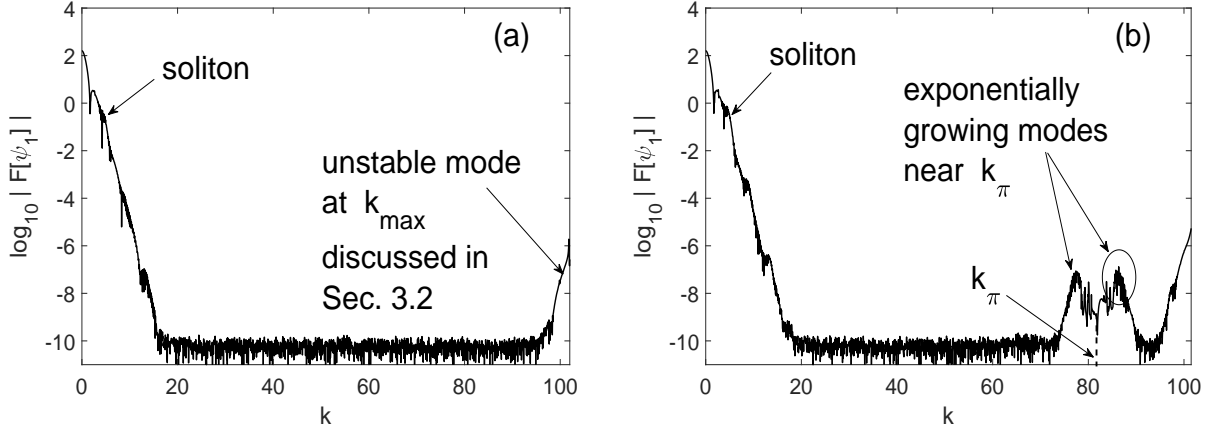
Figure 4: Numerical solution's spectrum for the initial soliton with $\Omega = 0.35$ (fragile). (Only the $k > 0$ part of the spectrum is shown for better visibility of details; the spectrum is symmetric about $k = 0$.) Simulation parameters are listed in the text, and: (a) $\Delta t = 0.9\Delta t_{\text{thresh}} \equiv 0.9\Delta x$; (b) $\Delta t = 1.25\Delta t_{\text{thresh}}$.

3.2 Unconditionally unstable modes near edges of spectral domain

As we mentioned in the previous paragraph, the modes referred to in the title of this subsection can be observed when the soliton is fragile. We have verified that, for the parameters of Fig. 4(a), such modes exist for Δt as small as 10^{-4}, i.e. $\Delta t < \Delta x/300$. In the analysis in Section 5 we will show that, indeed, such modes persist for $\Delta t \to 0$. As Ω increases, the growth rate of these modes decreases, and vice versa. This is illustrated in Fig. 5(a); note the different simulation times. This figure also illustrates another feature of these modes: two spikes that appear to be separated by approximately 2Ω. This feature is explained in Appendix C.
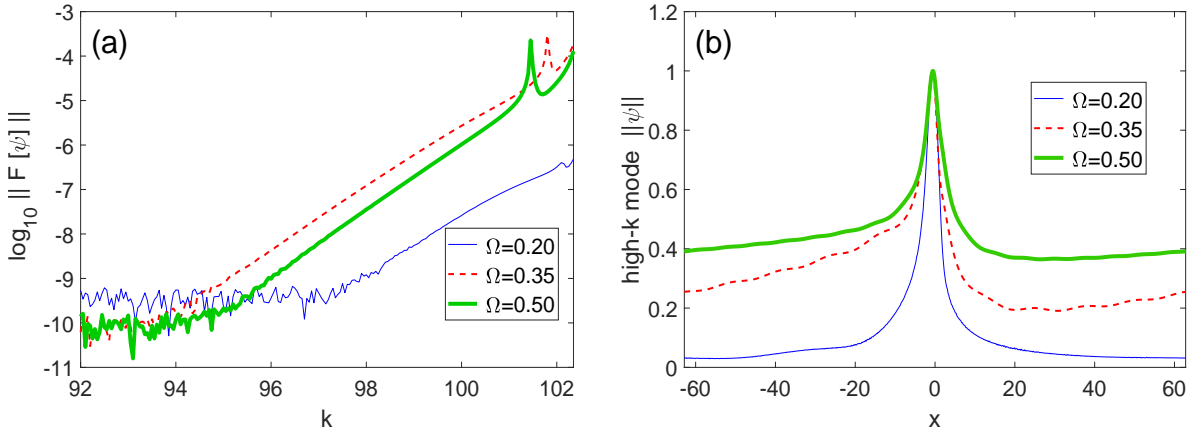

Figure 5: (a) Close-up on the spectrum near k_{max}. Note that simulation times were different, as follows: $t = 150$ for $\Omega = 0.2$; $t = 1500$ for $\Omega = 0.35$, and $t = 5000$ for $\Omega = 0.5$. Other simulation parameters are: $L = 40\pi$, $N = 2^{12}$ ($\Delta x \approx 0.031$), and $\Delta t = 0.01$. (b) The shape of the unstable modes in the x-domain, extracted from the results reported in (a) with a high-pass filter that extends from $k = 80$ to $k = k_{\text{max}}$. The modes' amplitudes are normalized to one. The notation $\|\cdots\|$ stands for the 2-norm of the corresponding two-component vector.

Applying gentle absorbing boundary conditions, as described in [25], was found to suppress these unstable modes for $\Omega = 0.35$ and 0.50, but not for 0.20. This observation is explained by Fig. 5(b), which shows that this mode becomes localized (albeit with slowly decaying 'tails') as Ω decreases. Clearly, absorbing boundary conditions can have only a relatively small effect on such a localized mode.

Finally, we verified that a significant increase (e.g., by a factor of 2 or more) of the computational domain does not affect the growth rate of the unconditionally unstable modes near k_{max} in any consistent way. This should be *contrasted* with the situation of numerically unstable modes that occur on the background of an NLS soliton: their growth rate decreases approximately as $1/L$ [19].

On the other hand, *similarly* to the NI for the NLS soliton, relatively small variations of L lead to *substantial* changes of the modes' growth rate. Moreover, they also lead to another unexpected behavior, which, along with the changes mentioned in the previous sentence, is described in the next subsection.

3.3 Unconditionally unstable "noise floor"

The spectrum of the numerical solution in Figs. 2 and 4 away from the soliton looks like a "floor". It appears approximately level because so is the spectrum of the white noise, which is added to the initial condition in all our simulations. Thus, we will refer to this part of the spectrum as the "noise floor". In this subsection we present numerical evidence that the "noise floor" can also become unconditionally unstable.

In Fig. 6(a) we show part of the spectrum of the numerical solution for parameters that are similar to those in Fig. 5: $\Omega = 0.35$, $N = 2^{12}$, $\Delta t = 0.01$ ($< \Delta t_{thresh}/3$), $t = 1500$, and four values of L in the vicinity of 40π. These results demonstrate that relatively small variation of L can suppress the growth of unstable modes near $\pm k_{max}$ and/or make the "noise floor" unstable. This NI is unconditional: reducing Δt to 0.001 left the results shown in Fig. 6 essentially unchanged. It is also not affected by varying N (for the same L). As Ω decreases (increases), the intervals of L values where the "noise floor" NI is observed expand (shrink).

In Fig. 6(b) we demonstrate that the "noise floor" NI is exponential. For the purposes of analysis in Section 6 we also show the growth of the same Fourier mode when instead of adding to the initial condition a small white noise, one adds the same small constant (on the order of 10^{-12}) to each Fourier mode. The analysis forthcoming in Section 6 will explain the observed staircase structure of the dashed curve in Fig. 6(b).

4 Setup of analysis, and dynamics of Fourier modes near $k_{m\pi}$

The main results of this section are Eqs. (26) and (27). They govern the evolution of the Fourier harmonics of a small and spectrally localized perturbatikon of the soliton with wavenumbers being far from (Eqs. (26)) and near (Eqs. (27)) the resonant wavenumbers (14). Equations (27) explain
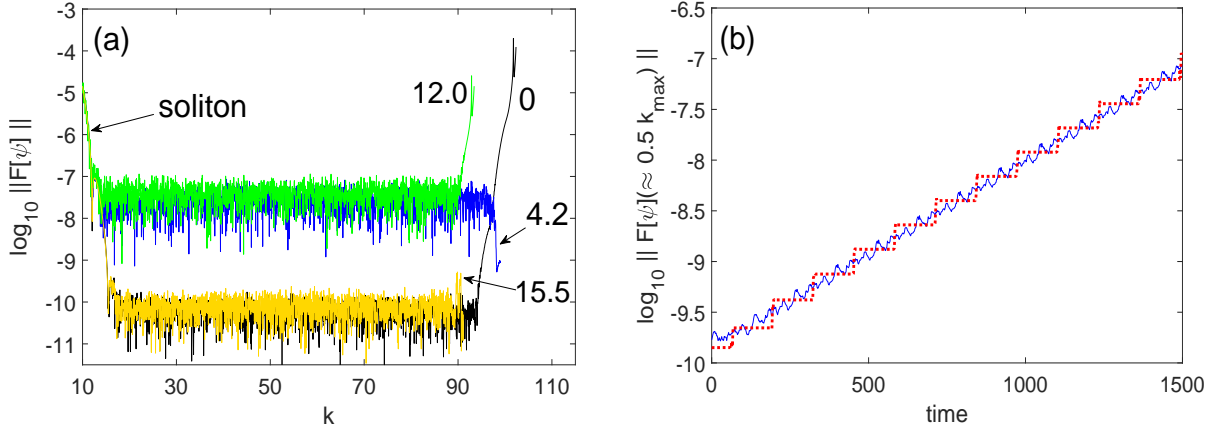
Figure 6: (a) Part of the numerical solution's spectrum focusing on the "noise floor". Simulation parameters are listed in the text, and the length of the computational domain is $L = 40\pi + \delta L$, with the value of δL labeling the corresponding curve. Four possible combinations, with the "noise floor" and the modes near $k_{\max}$ being (almost) stable or or unstable, are shown. (b) Evolution of the amplitude of the Fourier modes near $k = 60$ for the curve labeled with '4.2' in panel (a). Solid and dashed lines correspond to a small white noise or a constant, respectively, being added to each Fourier mode in the initial condition.

the numerical observations reported in Section 3.1. Moreover, the derivation steps carried out in this section are later used in the analyses of Sections 5 and 6 for different types of perturbations.

Stability of the second-order SSM (13) is the same as that of the first-order one,

$$
\begin{pmatrix} \psi_1 \\ \psi_2 \end{pmatrix} (x, t + \Delta t) = \exp\left[i(\Delta t)\mathcal{D}\right] \ \exp\left[i\Delta t \mathcal{N}\right] \begin{pmatrix} \psi_1 \\ \psi_2 \end{pmatrix} (x, t), \tag{15}
$$

because in the bulk of the calculation, the first and last $\mathcal{D} \ \Delta t/2$-substeps in (13) merge into one $\mathcal{D}$ Δt-substep in (15). Therefore, below we study stability of the SSM (15). Stability of a higher-order SSM can differ from that of the first- and second-order SSM [19]; however, this issue is outside the scope of this study.

We will require the definition of an N-point discrete Fourier transform and its inverse:

$$
\mathcal{F}[f(x)] \equiv \widehat{f}(k_l) = \sum_{j=-N/2}^{N/2-1} f(x_j) \, e^{-ik_l x_j} \, ; \qquad \mathcal{F}^{-1}[\widehat{f}(k)] \equiv f(x_j) = \frac{1}{N} \sum_{l=-N/2}^{N/2-1} \widehat{f}(k_l) \, e^{ik_l x_j} \, , \tag{16}
$$

with $k_l = l\Delta k \equiv 2\pi l/L$. Following [19], we consider stability of a numerical perturbation whose spectral content is localized near wavenumbers $\pm k_0$ for some $k_0 \gg 1$, $k_0 \lesssim k_{\max}$. Thus, the solution has the form (10), where the vector $\widetilde{\boldsymbol{\psi}}_{\{n\}}(x) \equiv \widetilde{\boldsymbol{\psi}}(x, n\Delta t)$, defined after that equation, is sought in the form:

$$
\widetilde{\boldsymbol{\psi}}_{\{n\}}(x) = \boldsymbol{\alpha}_{\{n\}}(x)e^{ik_0 x} + \boldsymbol{\beta}_{\{n\}}(x)e^{-ik_0 x}. \tag{17}
$$

Here we assume that the spectral width of $\boldsymbol{\alpha}$ and $\boldsymbol{\beta}$ is of order one and hence is much smaller than k_0; therefore, the two terms in (17) are well separated in the Fourier space. Note that here and everywhere below, the subscript in curly brackets, such as $\{n\}$, denotes the time level $n\Delta t$, whereas

13

subscripts without curly brackets denote either indices of Fourier harmonics, as in (16), or partial differentiation, as in (1) or (2), depending on the context.

Substitution of (10) and (17) into (15), subsequent linearization, and taking the Fourier transform result in:

$$|k-k_0| = O(1): \qquad \mathcal{F}\left[\boldsymbol{\alpha}_{\{n+1\}}\, e^{ik_0 x}\right] e^{-i\Omega\Delta t} \;=\; e^{-i\boldsymbol{\sigma}_1 k\Delta t}\, \mathcal{F}\left[\boldsymbol{\alpha}_{\{n\}} e^{ik_0 x} + i\Delta t\left(\boldsymbol{P}\boldsymbol{\alpha}_{\{n\}} + \boldsymbol{Q}\boldsymbol{\beta}^*_{\{n\}}\right)e^{ik_0 x}\right],$$
$$\text{(18a)}$$

$$|k+k_0| = O(1): \qquad \mathcal{F}\left[\boldsymbol{\beta}_{\{n+1\}}\, e^{-ik_0 x}\right] e^{-i\Omega\Delta t} \;=\; e^{-i\boldsymbol{\sigma}_1 k\Delta t}\, \mathcal{F}\left[\boldsymbol{\beta}_{\{n\}} e^{-ik_0 x} + i\Delta t\left(\boldsymbol{P}\boldsymbol{\beta}_{\{n\}} + \boldsymbol{Q}\boldsymbol{\alpha}^*_{\{n\}}\right)e^{-ik_0 x}\right],$$
$$\text{(18b)}$$

where $\boldsymbol{P}$ and $\boldsymbol{Q}$ are defined in (11), and

$$e^{-i\boldsymbol{\sigma}_1 k\Delta t} \equiv \boldsymbol{\sigma}_0 \cos(k\Delta t) - i\boldsymbol{\sigma}_1 \sin(k\Delta t). \tag{19}$$

Here and below we suppress the explicit dependence of $\boldsymbol{\alpha}_{\{n\}}$, $\boldsymbol{\beta}_{\{n\}}$ etc. on x. Next, in (18a), one writes $\exp[-i\boldsymbol{\sigma}_1 k\Delta t] = \exp[-i\boldsymbol{\sigma}_1 k_0\Delta t]\,\exp[-i\boldsymbol{\sigma}_1(k-k_0)\Delta t]$ and takes the inverse Fourier transform to obtain:

$$\boldsymbol{\alpha}_{\{n+1\}}\, e^{-i\Omega\Delta t} \;=\; e^{-i\boldsymbol{\sigma}_1 k_0\Delta t}\left(\boldsymbol{\alpha}_{\{n\}} - \Delta t\boldsymbol{\sigma}_1\boldsymbol{\alpha}_{\{n\},\,x} + i\Delta t(\boldsymbol{P}\boldsymbol{\alpha}_{\{n\}} + \boldsymbol{Q}\boldsymbol{\beta}^*_{\{n\}})\right) + O(\Delta t^2). \tag{20a}$$

Indeed, since $|k-k_0|\Delta t \ll 1$, we have approximated $\mathcal{F}^{-1}\big[\,\exp[-i\boldsymbol{\sigma}_1(k-k_0)\Delta t]\,\mathcal{F}\big[\boldsymbol{\alpha}_{\{n\}}\exp[ik_0 x]\big]\,\big]$ by

$$\mathcal{F}^{-1}\left[(\boldsymbol{\sigma}_0 - i\boldsymbol{\sigma}_1(k-k_0)\Delta t)\,\mathcal{F}\left[\boldsymbol{\alpha}_{\{n\}}e^{ik_0 x}\right]\right] = \boldsymbol{\alpha}_{\{n\}}e^{ik_0 x} - \boldsymbol{\sigma}_1(\partial_x - ik_0)\left(\boldsymbol{\alpha}_{\{n\}}e^{ik_0 x}\right) = \left(\boldsymbol{\alpha}_{\{n\}} - \boldsymbol{\sigma}_1\boldsymbol{\alpha}_{\{n\},\,x}\right)e^{ik_0 x}$$

and $\Delta t\,\exp[-i\boldsymbol{\sigma}_1(k-k_0)\Delta t]$ by Δt with accuracy $O(\Delta t)$. Similarly, and omitting $O(\Delta t^2)$ terms, one obtains from (18b):

$$\boldsymbol{\beta}_{\{n+1\}}\, e^{-i\Omega\Delta t} \;=\; e^{i\boldsymbol{\sigma}_1 k_0\Delta t}\left(\boldsymbol{\beta}_{\{n\}} - \Delta t\boldsymbol{\sigma}_1\boldsymbol{\beta}_{\{n\},\,x} + i\Delta t(\boldsymbol{P}\boldsymbol{\beta}_{\{n\}} + \boldsymbol{Q}\boldsymbol{\alpha}^*_{\{n\}})\right). \tag{20b}$$

Since $k_0 \ll 1$, the factors $\exp[\mp i\boldsymbol{\sigma}_1 k_0\Delta t]$ dominate the evolutions of $\boldsymbol{\alpha}_n$ and $\boldsymbol{\beta}_n$. Accordingly, we use the standard perturbation theory approach and seek solutions of (20) in the form:

$$\boldsymbol{\alpha}_{\{n\}} = \left(\boldsymbol{a}^{(0)}_{\{n\}} + \boldsymbol{a}^{(1)}_{\{n\}}\right) e^{-in\boldsymbol{\sigma}_1 k_0\Delta t}, \qquad \boldsymbol{\beta}_{\{n\}} = \left(\boldsymbol{b}^{(0)}_{\{n\}} + \boldsymbol{b}^{(1)}_{\{n\}}\right) e^{in\boldsymbol{\sigma}_1 k_0\Delta t}, \tag{21a}$$

where $\boldsymbol{a}^{(0)}_{\{n\}}$, $\boldsymbol{b}^{(0)}_{\{n\}}$ vary with n slowly compared to $\exp[\mp i\boldsymbol{\sigma}_1 k_0\Delta t]$, and

$$\left\{|\boldsymbol{a}^{(1)}_{\{n\}}|,\; |\boldsymbol{b}^{(1)}_{\{n\}}|\right\} = O\left(\Delta t\cdot\left\{|\boldsymbol{a}^{(0)}_{\{n\}}|,\; |\boldsymbol{b}^{(0)}_{\{n\}}|\right\}\right) \qquad \forall n. \tag{21b}$$

Substituting (21) into (20a), multiplying both sides by $\exp[i(n+1)\boldsymbol{\sigma}_1 k_0\Delta t]$, and again discarding $O(\Delta t^2)$ terms, one has:

$$\boldsymbol{a}^{(0)}_{\{n+1\}}(1 - i\Omega\Delta t) + \boldsymbol{a}^{(1)}_{\{n+1\}} \;=\; \boldsymbol{a}^{(0)}_{\{n\}} - \Delta t\boldsymbol{\sigma}_1\boldsymbol{a}^{(0)}_{\{n\},\,x} + \boldsymbol{a}^{(1)}_{\{n\}} + \tag{22}$$
$$i\Delta t\left[\left(\boldsymbol{P}_{01} + \boldsymbol{P}_{23}e^{-2i(n+1)\boldsymbol{\sigma}_1 k_0\Delta t}\right)\boldsymbol{a}^{(0)}_{\{n\}} + \left(\boldsymbol{Q}_{01} + \boldsymbol{Q}_{23}e^{-2i(n+1)\boldsymbol{\sigma}_1 k_0\Delta t}\right)(\boldsymbol{b}^{(0)}_{\{n\}})^*\right].$$

Here $\boldsymbol{P}_{jl} \equiv \boldsymbol{\sigma}_j P_j + \boldsymbol{\sigma}_l P_l$ and similarly for $\boldsymbol{Q}_{jl}$, and we have used the identity

$$e^{i\boldsymbol{\sigma}_1 s} \boldsymbol{\sigma}_j e^{-i\boldsymbol{\sigma}_1 s} = \boldsymbol{\sigma}_j e^{-2i\boldsymbol{\sigma}_1 s}, \qquad j = 2, 3, \tag{23}$$

which follows from the anti-commutation of $\boldsymbol{\sigma}_1$ with $\boldsymbol{\sigma}_{2,3}$. A similar equation holds for $\boldsymbol{b}^{(0),(1)}$.

Subsequent analysis of these equations depends on whether $k_0 = k_{m\pi}$ for some $m \in \mathbb{N}$. To set up analyses in Sections 5 and 6, we first consider the case where $k_0 \neq k_{m\pi}$ (more generally, this is $|k_0 - k_{m\pi}| \gg 1$: see (18a)). Then terms in (22) which are proportional to $\boldsymbol{a}^{(0)}$ and $(\boldsymbol{b}^{(0)})^*$ split into two groups: fast-oscillating (proportional to $\exp[-2i(n+1)\boldsymbol{\sigma}_1 k_0 \Delta t]$) and those varying slowly with n. If the latter terms do not all cancel out, they will drive the $\boldsymbol{a}^{(1)}_{\{n\}}$-term, which therefore will grow, and condition (21b) will eventually be violated. To prevent this from occurring, one requires that all these slowly varying terms cancel out, yielding:

$$\boldsymbol{a}^{(0)}_{\{n+1\}}(1 - i\Omega \Delta t) = (\boldsymbol{\sigma}_0 - \Delta t \boldsymbol{\sigma}_1 \partial_x)\boldsymbol{a}^{(0)}_{\{n\}} + i\Delta t \left(\boldsymbol{P}_{01} \boldsymbol{a}^{(0)}_{\{n\}} + \boldsymbol{Q}_{01}(\boldsymbol{b}^{(0)}_{\{n\}})^* \right). \tag{24a}$$

The remaining terms provide an equation for $\boldsymbol{a}^{(1)}$:

$$\boldsymbol{a}^{(1)}_{\{n+1\}} - \boldsymbol{a}^{(1)}_{\{n\}} = \Delta t \, e^{-2i(n+1)\boldsymbol{\sigma}_1 k_0 \Delta t} \boldsymbol{c}_{\{n\}}, \qquad \boldsymbol{c}_{\{n\}} \equiv \boldsymbol{P}_{23} \boldsymbol{a}^{(0)}_{\{n\}} + \boldsymbol{Q}_{23}(\boldsymbol{b}^{(0)}_{\{n\}})^*; \tag{24b}$$

note that $\boldsymbol{c}_{\{n\}}$ varies slowly with n. Due to this fact and the presence of a fast-varying exponential on the r.h.s. of (24b), the solution of that equation does not grow with n, and hence condition (21b) holds. Thus, since the terms $\boldsymbol{a}^{(1)}$, $\boldsymbol{b}^{(1)}$ remain small compared to $\boldsymbol{a}^{(0)}$, $\boldsymbol{b}^{(0)}$ at all times, we will no longer consider the former terms and will focus on the latter. Taking into account the slow dependence of $\boldsymbol{a}^{(0)}_{\{n\}}$ on n, we approximate

$$\boldsymbol{a}^{(0)}_{\{n+1\}} = \boldsymbol{a}^{(0)}_{\{n\}} + \Delta t (\partial_t \boldsymbol{a}^{(0)})_{\{n\}} + O(\Delta t^2). \tag{25}$$

Finally, substituting (25) into (24a) and omitting (Δt^2) terms, we obtain:

$$\boldsymbol{a}_t + \boldsymbol{\sigma}_1 \boldsymbol{a}_x - i\Omega \boldsymbol{a} = i\boldsymbol{P}_{01} \boldsymbol{a} + i\boldsymbol{Q}_{01} \boldsymbol{b}^*. \tag{26a}$$

Here and below we will omit the superscipt (0) of $\boldsymbol{a}$ and $\boldsymbol{b}$. Similar calculations yield the equation for $\boldsymbol{b}$:

$$\boldsymbol{b}_t + \boldsymbol{\sigma}_1 \boldsymbol{b}_x - i\Omega \boldsymbol{b} = i\boldsymbol{Q}_{01} \boldsymbol{a}^* + i\boldsymbol{P}_{01} \boldsymbol{b}. \tag{26b}$$

We will return to the derivation in this paragraph in Sections 5 and 6.

Now, in the case $k_0 = k_{m\pi}$, since $2k_0 \Delta t = 2m\pi$, all terms in (22) vary slowly with n. (This also holds for $|k_0 - k_{m\pi}| = O(1)$, since we can use the freedom in (17), which requires only that $\boldsymbol{\alpha}$ and $\boldsymbol{\beta}$ vary in x on the scale of order one.) Following the derivation in the previous paragraph, one obtains, instead of (26), equations:

$$\boldsymbol{a}_t + \boldsymbol{\sigma}_1 \boldsymbol{a}_x - i\Omega \boldsymbol{a} = i\boldsymbol{P}\boldsymbol{a} + i\boldsymbol{Q}\boldsymbol{b}^*. \tag{27a}$$

$$\boldsymbol{b}_t + \boldsymbol{\sigma}_1 \boldsymbol{b}_x - i\Omega \boldsymbol{b} = i\boldsymbol{Q}\boldsymbol{a}^* + i\boldsymbol{P}\boldsymbol{b}. \tag{27b}$$

Thus, the vector $(\boldsymbol{a}^T, (\boldsymbol{b}^*)^T)^T$, representing a *numerical* perturbation that is spectrally localized near $k_{m\pi}$, satisfies the same equation (12) that governs the evolution of the *physical* (i.e., low-wavenumber) perturbation to the soliton. Thus, modes near $k_{m\pi}$ have the same stability properties as the low-wavenumber modes. In other words, NI near $k_{m\pi}$ occurs if and only if small physical (i.e., low-k) perturbations of the soliton grow exponentially (i.e., if the soliton (8) is fragile). This provides the analytical ground for the numerical observations made in Section 3.1 and Appendix B.

5   Unconditional numerical instability near $|k| = k_{\max}$

In this section we will present a theory explaining the numerical results of Section 3.2. This will be accomplished by numerically solving the eigenvalue problem (34).

A numerical perturbation whose spectral content is concentrated near the edges of the computational domain is sought in the form (17), where now $k_0 = k_{\max}$ and, in addition, the Fourier transform of $\boldsymbol{\alpha}(x)$ (of $\boldsymbol{\beta}(x)$) contains harmonics with only negative (respectively, nonnegative) wavenumbers:

$$\boldsymbol{\alpha}(x) = \sum_{l=1}^{M} \widehat{\boldsymbol{\alpha}}_l \, e^{-ik_l x}, \qquad \boldsymbol{\beta}(x) = e^{-\Delta k x} \sum_{l=1}^{M} \widehat{\boldsymbol{\beta}}_l \, e^{ik_l x}, \tag{28}$$

where $1 \ll M \ll N/2$. The last strong inequality holds because the spectral content of the perturbation is concentrated near the edges of the spectral domain. Recall that the computational spectral window is $k_l \in [-k_{\max}, k_{\max} - \Delta k]$, where $k_{\max}$ is defined in (4c) and k_l, Δk are defined after (16).

When we substitute Eqs. (17) with (28) into (15), then, similarly to the r.h.s. of (18), we obtain terms like $\boldsymbol{P}\boldsymbol{\alpha} \exp[ik_{\max}x]$ etc.. Note, however, that the coefficient $\boldsymbol{P}(x)\boldsymbol{\alpha}(x)$ had Fourier harmonics with wavenumbers of both signs, due to $\boldsymbol{P}(x)$ having such harmonics. Therefore, such terms are to be split into two groups:

$$\boldsymbol{P}\boldsymbol{\alpha} \equiv [\boldsymbol{P}\boldsymbol{\alpha}]^{(<0)} + [\boldsymbol{P}\boldsymbol{\alpha}]^{(\geq 0)}, \tag{29a}$$

where the superscript indicates what Fourier harmonics the term has. When multiplied by $\exp[ik_{\max}x]$, the former group of terms on the r.h.s. of (29a) will have the spectral content near the right edge of the spectral domain, while the latter group's spectral content will "spill over" to the left edge due to aliasing. Thus,

$$\boldsymbol{P}\boldsymbol{\alpha} \, e^{ik_{\max}x} = [\boldsymbol{P}\boldsymbol{\alpha}]^{(<0)} \, e^{ik_{\max}x} + [\boldsymbol{P}\boldsymbol{\alpha}]^{(\geq 0)} \, e^{-ik_{\max}x}. \tag{29b}$$

With this observation in mind, the counterparts of Eqs. (18) near the edges of the spectral domain become:

$$\widehat{\boldsymbol{\alpha}}_{\{n+1\}} \, e^{i\boldsymbol{\sigma}_1(k_{\max} + \delta k^{(<0)})\Delta t - i\Omega\Delta t} = \widehat{\boldsymbol{\alpha}}_{\{n\}} + i\Delta t \, \mathcal{F}\left[\left[\boldsymbol{P}\left(\boldsymbol{\alpha}_{\{n\}} + \boldsymbol{\beta}_{\{n\}}\right) + \boldsymbol{Q}\left(\boldsymbol{\alpha}^*_{\{n\}} + \boldsymbol{\beta}^*_{\{n\}}\right)\right]^{(<0)}\right],$$
$$\tag{30a}$$

$$\widehat{\boldsymbol{\beta}}_{\{n+1\}} \, e^{i\boldsymbol{\sigma}_1(-k_{\max}+\delta k^{(\geq 0)})\Delta t - i\Omega\Delta t} \; = \; \widehat{\boldsymbol{\beta}}_{\{n\}} + i\Delta t \, \mathcal{F}\left[\left[\boldsymbol{P}\left(\boldsymbol{\alpha}_{\{n\}} + \boldsymbol{\beta}_{\{n\}}\right) + \boldsymbol{Q}\left(\boldsymbol{\alpha}^*_{\{n\}} + \boldsymbol{\beta}^*_{\{n\}}\right)\right]^{(\geq 0)}\right],$$

$$\text{(30b)}$$

where

$$\delta k^{(<0)} = k - k_{\max} < 0, \qquad \delta k^{(\geq 0)} = k + k_{\max} \geq 0.$$

Note that all Fourier transforms in (30a) (in (30b)) are evaluated at $\delta k^{(<0)}$ (respectively, at $\delta k^{(\geq 0)}$).

In Section 4 we were able to take the inverse Fourier transform of Eqs. (18), which are counterparts of Eqs. (30), and proceed with the analysis in the x-space. In the case of Eqs. (30), this would result not in differential equations, such as (26) or (27), but in integro-differential ones, due to the separation of positive and negative wavenumbers on the r.h.s. of (30). Quantitative analysis of such integro-differential equations would be more difficult than analysis of the original Fourier-space equations (30). Therefore, below we will proceed with the latter analysis. Yet, those integro-differential equations still allow one to *qualitatively* explain the two-peak feature of the unstable modes seen in Fig. 5(a); therefore, we briefly discuss them in Appendix C.

Following the derivation of Eqs. (26), except for not taking the inverse Fourier transform, one obtains from (30):

$$\widehat{\boldsymbol{a}}_t \; = \; i\left(\boldsymbol{\sigma}_0\Omega - \boldsymbol{\sigma}_1\delta k^{(<0)}\right)\widehat{\boldsymbol{a}} + i\,\mathcal{F}\left[[\boldsymbol{P}_{01}\boldsymbol{a} + \boldsymbol{P}_{23}\boldsymbol{b} + \boldsymbol{Q}_{23}\boldsymbol{a}^* + \boldsymbol{Q}_{01}\boldsymbol{b}^*]^{(<0)}\right], \qquad \text{(31a)}$$

$$\widehat{\boldsymbol{b}}_t \; = \; i\left(\boldsymbol{\sigma}_0\Omega - \boldsymbol{\sigma}_1\delta k^{(\geq 0)}\right)\widehat{\boldsymbol{b}} + i\,\mathcal{F}\left[[\boldsymbol{P}_{23}\boldsymbol{a} + \boldsymbol{P}_{01}\boldsymbol{b} + \boldsymbol{Q}_{01}\boldsymbol{a}^* + \boldsymbol{Q}_{23}\boldsymbol{b}^*]^{(\geq 0)}\right]. \qquad \text{(31b)}$$

Using the same justification as in (26), we have neglected small terms $\widehat{\boldsymbol{a}}^{(1)}$, $\widehat{\boldsymbol{b}}^{(1)}$ and omitted the superscript (0). System (31) determines stability of a $8M$-dimensional vector: M harmonics in each of the two-component vectors $\widehat{\boldsymbol{a}}$ and $\widehat{\boldsymbol{b}}$ are coupled with as many harmonics of their complex conjugates. It is possible to halve the size of the involved vectors (i.e., from $8M$ to $4M$) by means of the following substitution:

$$\widehat{\boldsymbol{a}} = \widehat{a}_{(+)}\boldsymbol{e}_{(+)} + \widehat{a}_{(-)}\boldsymbol{e}_{(-)}, \qquad \widehat{\boldsymbol{b}} = \widehat{b}_{(+)}\boldsymbol{e}_{(+)} + \widehat{b}_{(-)}\boldsymbol{e}_{(-)}, \qquad \boldsymbol{e}_{(\pm)} \equiv \begin{pmatrix} 1 \\ \pm 1 \end{pmatrix}; \qquad \text{(32)}$$

the same decomposition also holds for $\boldsymbol{a}$ and $\boldsymbol{b}$. Vectors $\boldsymbol{e}_{(\pm)}$ satisfy the following relations:

$$\boldsymbol{\sigma}_0\boldsymbol{e}_{(\pm)} = \boldsymbol{e}_{(\pm)}, \quad \boldsymbol{\sigma}_1\boldsymbol{e}_{(\pm)} = \pm\boldsymbol{e}_{(\pm)}, \quad \boldsymbol{\sigma}_2\boldsymbol{e}_{(\pm)} = \mp i\boldsymbol{e}_{(\mp)}, \quad \boldsymbol{\sigma}_3\boldsymbol{e}_{(\pm)} = \boldsymbol{e}_{(\mp)}. \qquad \text{(33)}$$

Substituting (32) into (31) and using relations (33), one can see that harmonics $\widehat{a}_{(+)}$ are coupled with harmonics $\widehat{b}_{(-)}$, $\widehat{a}^*_{(-)}$, and $\widehat{b}^*_{(+)}$. The corresponding equations are found in Appendix C; here we will present only their matrix form, which is needed for a stability analysis. Defining M-dimensional column vectors, e.g.: $\underline{\widehat{a}}_{(+)} = \left[(\widehat{a}_{(+)})_1, \ldots, (\widehat{a}_{(+)})_M\right]^T$, etc., where the numeric subscript denotes the harmonic's number (see (28)) and 'T' denotes the transpose, one can write the system that results from (31)–(33) in the form:

$$\underline{\underline{\mathbb{s}}}_t \; = \; i\,(\mathbb{D} + \mathbb{C})\,\underline{\underline{\mathbb{s}}}, \qquad \text{(34a)}$$

where:

$$\mathbb{D} = \begin{pmatrix} \Delta k \, \mathbb{M} + \Omega \, \mathbb{I} & 0 & 0 & 0 \\ 0 & \Delta k (\mathbb{M} - \mathbb{I}) + \Omega \, \mathbb{I} & 0 & 0 \\ 0 & 0 & \Delta k \, \mathbb{M} - \Omega \, \mathbb{I} & 0 \\ 0 & 0 & 0 & \Delta k (\mathbb{M} - \mathbb{I}) - \Omega \, \mathbb{I} \end{pmatrix}, \qquad (34\text{b})$$

$$\underline{\mathfrak{s}} = \begin{pmatrix} \widehat{\underline{a}}_{(+)} \\ \widehat{\underline{b}}_{(-)} \\ \widehat{\underline{a}}^*_{(-)} \\ \widehat{\underline{b}}^*_{(+)} \end{pmatrix}, \qquad \mathbb{C} = \frac{1}{N} \begin{pmatrix} \mathbb{C}_{11} & \mathbb{C}_{12} & \mathbb{C}_{13} & \mathbb{C}_{14} \\ \mathbb{C}_{21} & \mathbb{C}_{22} & \mathbb{C}_{23} & \mathbb{C}_{24} \\ \mathbb{C}_{31} & \mathbb{C}_{32} & \mathbb{C}_{33} & \mathbb{C}_{34} \\ \mathbb{C}_{41} & \mathbb{C}_{42} & \mathbb{C}_{43} & \mathbb{C}_{44} \end{pmatrix}, \qquad (34\text{c})$$

N is the total number of grid points in the computational domain (see (16)); $\mathbb{I}$ is the $M \times M$ identity matrix; $\mathbb{M} = \text{diag}\,[1 : M]$ is the $M \times M$ diagonal matrix with integer entries; and the $M \times M$ blocks $\mathbb{C}_{jm}$, which appear from the convolution-like terms on the r.h.s. of (31), are written out explicitly in Appendix D. Each of these blocks has a logically clear structure and can be easily programmed.

The stability analysis of system (34) is straightforward: one seeks $\underline{\mathfrak{s}}$ proportional to $\exp[\lambda t]$, whence the system becomes a $4M \times 4M$ eigenvalue problem. For $M \sim 100$, it is solved by Matlab in about 1 second. Eigenvalues with $\text{Re}\lambda > 0$ correspond to numerically unstable modes, which, by design, occur near the edges of the computational spectrum. In Fig. 7 we show the unstable eigenvectors of that system corresponding to the solitons with the three values of Ω for which graphs are shown in Fig. 5(a). One can see a good agreement between the spectral profiles of the unstable modes in that figure and their counterparts in Fig. 7(d)–(f). Furthermore, in Fig. 8 we show the NI growth rate (i.e., max $\text{Re}\lambda$) versus the length L of the computational domain for the same three values of Ω. The values obtained from the preceding analysis match closely the corresponding values measured in direct numerical simulations, thus *validating our analysis*.

Three clarifications about Fig. 8 are in order. First, the dependence of the eigensolutions of problem (34) on L occur only via $\Delta k = 2\pi/L$. Second, the rather sharp "bounces" of the eigenvalues with L occur due to mode competition. We have observed that unstable modes look like either as shown in Fig. 7 or as "peaks" both of which a separated from $\delta k = 0$ by an amount of order 1. As L varies, a mode from one group that has been dominant is "overcome" by a mode from the other group, and this switching of the dominant mode between the two groups goes on intermittently.

Third, the growth rate deduced from direct numerical simulations was computed as follows. For a given Ω, the simulations were run up to the respective time indicated in the caption to Fig. 5. The temporal evolution of the logarithm of the maximum amplitude of Fourier harmonics in some vicinity of $k = k_{\max}$ was plotted, as in Fig. 3(b). After some transitional period, akin to that in the solid curve in Fig. 3(a), that evolution became (approximately) linear in the logarithmic scale, similar to that in Fig. 3(b). The growth rate was deduced from the slope of that linear section.

Finally, in Fig. 9 we also show the NI growth rate as a function of L of a non-fragile soliton with $\Omega = 0.75$. Again, a good agreement between our analysis and direct numerics is seen. Moreover,
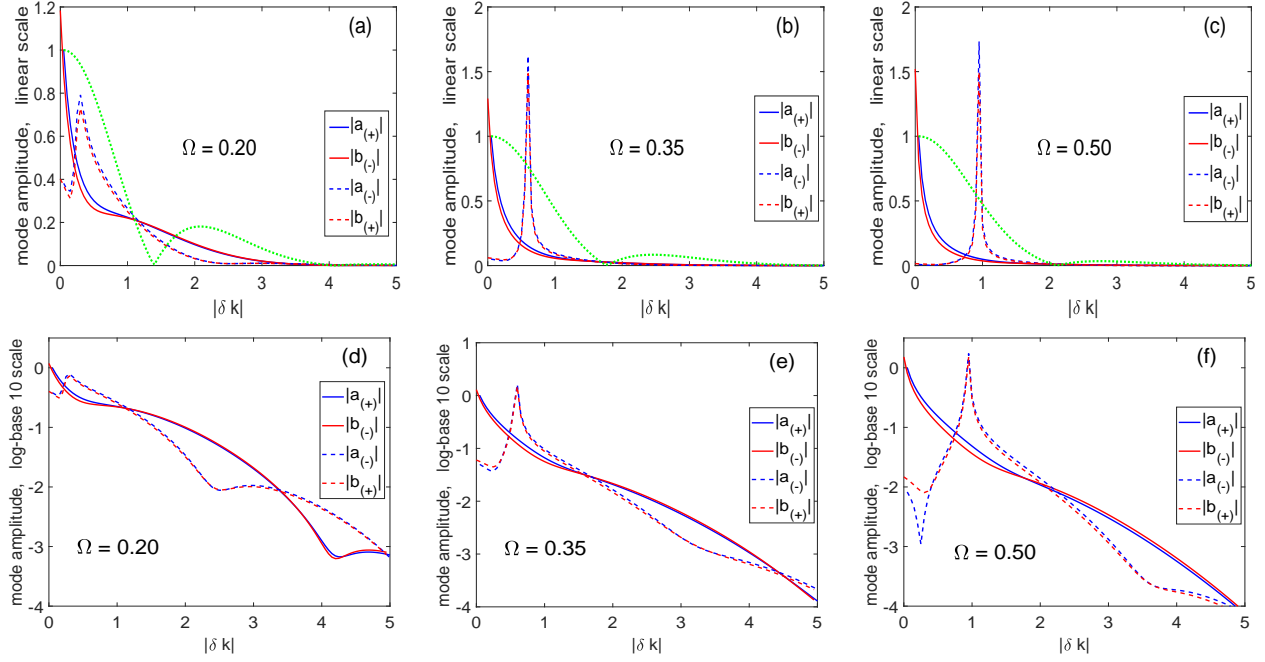
18

Figure 7: (Color online) Shapes of the most unstable eigenvectors of (34), $\left|\widehat{\underline{a}}_{(\pm)}\right|$ vs. $\delta k^{(<0)}$ and $\left|\widehat{\underline{b}}_{(\pm)}\right|$ vs. $\delta k^{(\geq 0)}$, for the solitons with the same values of Ω as shown in Fig. 5(a). Panels (a)–(c): linear scale; panels (d)–(f): logarithmic scale. All eigenvectors are normalized to $\max\left|\widehat{\underline{a}}_{(+)}\right|$. In (a)–(c), the dotted green line shows $\widehat{P}_0(k)$, normalized to 1, for comparison.
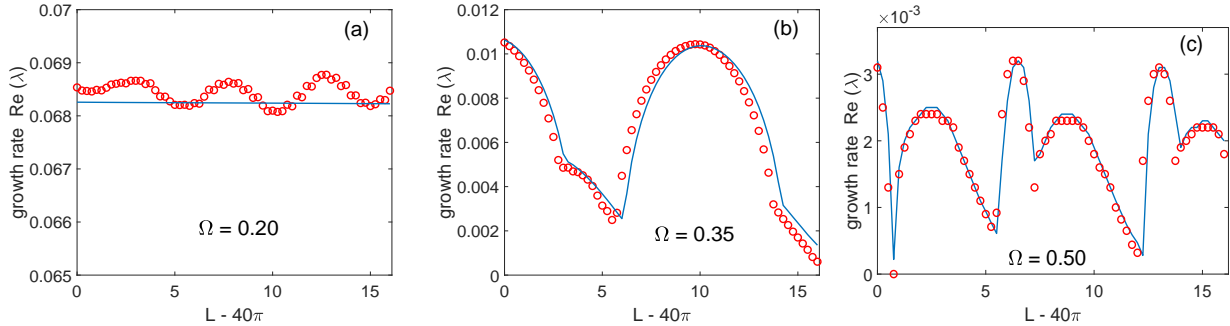

Figure 8: Growth rate of the most unstable mode of eigenvalue problem (34) as the function of length L of the computational domain. Note that in the three panels, corresponding to the values of Ω used in Fig. 7, the vertical scales are all drastically different. Solid lines correspond to the solution of (34) while circles are the result of direct numerical simulation with the SSM. See text for details.

Fig. 9 demonstrates that the SSM can be unconditionally unstable even for non-fragile solitons; it is just that in that case, the instability is so weak that it will not affect simulations for most realistic simulation times.

6 Unconditional instability of the "noise floor"

The main result of this section is based on Eq. (45), which describes the evolution of the "noise floor" amplitude. The growth rate of the "noise floor" is found from the spectral radius of the
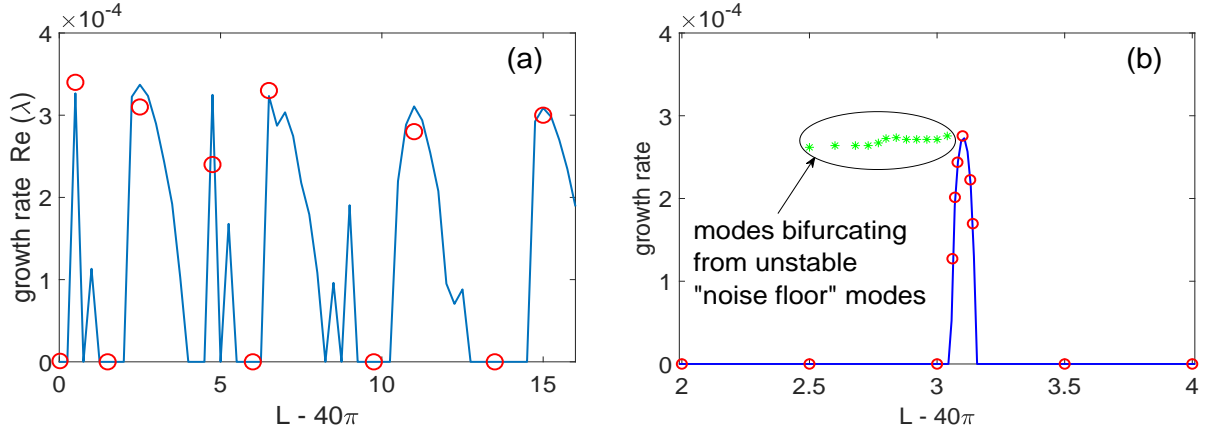
Figure 9: Parameters for both panels: $\Omega = 0.75$, simulation time $t = 50,000$, $N = 2^{12}$, and $\Delta t = \Delta x/5$. Panel (a): Growth rate of the most unstable mode of eigenvalue problem (34) as the function of length L of the computational domain. Solid line corresponds to the solution of (34) for $L \in [40\pi, 40\pi + 16]$ with increment $\Delta L = 0.25$. (Using a smaller ΔL in this case, unlike those in Fig. 8, would reveal even faster changes of the growth rate.) Circles are the results of direct numerical simulations with the SSM. Due to the growth rate being an order of magnitude smaller than for $\Omega = 0.50$, the simulation time used had to be proportionally greater; due to this large simulation time, the simulations were run only for the major "peaks" and for the midpoints of the intervals where the theory predicts zero growth rate. Panel (b): Growth rate of the "noise floor" as the function of length L of the computational domain. Solid line corresponds to the analysis presented in Section 6, while circles are the results of direct numerical simulations with the SSM. The period (in L) of this growth rate is $2\pi/(2\Omega) \approx 4.2$, and therefore we performed computations only for $L \in [40\pi, 40\pi + 4.2]$. Both analysis and numerics show no "noise floor" NI for $L \in [40\pi, 40\pi + 2]$, and therefore we present here only the other part of this interval. The numerical results shown with stars pertain to a NI related to, but different from, the "noise floor" and discussed in Appendix F. The reason for not showing these results for $L < 40\pi + 2.5$ is explained there.

corresponding fundamental solution, defined in (46b).

To study the "noise floor" NI, described in Section 3.3 and illustrated in Fig. 6, one cannot use ansatz (17). Indeed, a perturbation described by the "noise floor" is not spectrally narrow and hence is not a slowly-modulated plane wave in the x-space; see the sentence after (17). Instead, we will consider the most general form of a perturbation:

$$\widetilde{\psi}_{\{n\}}(x) = \sum_j \widehat{\alpha}_{j,\{n\}} e^{ik_j x} + \widehat{\beta}_{j,\{n\}} e^{-ik_j x}, \qquad (35a)$$

where the double subscript in (35) stands for a Fourier harmonic at wavenumber k_j and time level $n\Delta t$; a similar notation will be employed below in this section. The summation here is assumed over the harmonics of the "noise floor", i.e. those with

$$k_j \gg 1 \quad \text{and} \quad (k_{\max} - k_j) \gg 1. \qquad (35b)$$

The first inequality in (35b) ensures that the harmonics are outside the spectrum of the back-

20

ground soliton, whereas the second one ensures that they are sufficiently far from the edges of the spectral domain. While the derivation of the equations predicting unstable dynamics of $\widehat{\boldsymbol{\alpha}}_j$ and $\widehat{\boldsymbol{\beta}}_j$ will generally follow the derivation of Section 4, we will specifically emphasize places where key differences occur.

Once one substitutes (10) and (35) into (15) and linearizes, one obtains equations analogous to (18):

$$\widehat{\boldsymbol{\alpha}}_{j,\,\{n+1\}} e^{-i\Omega\Delta t} = e^{-ik_j\boldsymbol{\sigma}_1\Delta t}\left(\widehat{\boldsymbol{\alpha}}_{j,\,\{n\}} + \frac{i\Delta t}{N}\sum_l \widehat{\boldsymbol{P}}_l\widehat{\boldsymbol{\alpha}}_{j-l,\,\{n\}} + \widehat{\boldsymbol{Q}}_l(\widehat{\boldsymbol{\beta}}_{j-l,\,\{n\}})^*\right), \qquad (36a)$$

$$\widehat{\boldsymbol{\beta}}_{j,\,\{n+1\}} e^{-i\Omega\Delta t} = e^{ik_j\boldsymbol{\sigma}_1\Delta t}\left(\widehat{\boldsymbol{\beta}}_{j,\,\{n\}} + \frac{i\Delta t}{N}\sum_l \widehat{\boldsymbol{Q}}_l(\widehat{\boldsymbol{\alpha}}_{j+l,\,\{n\}})^* + \widehat{\boldsymbol{P}}_l\widehat{\boldsymbol{\beta}}_{j+l,\,\{n\}}\right). \qquad (36b)$$

The sums on the r.h.s. of these equations were obtained similarly to those in (D.1) and (D.3); however, for a reason that will become clear soon, the indices were switched between the $\widehat{\boldsymbol{P}}, \widehat{\boldsymbol{Q}}$ and the $\widehat{\boldsymbol{\alpha}}, \widehat{\boldsymbol{\beta}}$ terms. Since the spectral width of the background soliton is $O(1)$, the summation in (36) effectively extends over $O(1)/\Delta k \ll N$ indices.

Similarly to (21), one seeks

$$\widehat{\boldsymbol{\alpha}}_{j,\{n\}} = \left(\widehat{\boldsymbol{a}}_{j,\{n\}}^{(0)} + \widehat{\boldsymbol{a}}_{j,\{n\}}^{(1)}\right) e^{-in\boldsymbol{\sigma}_1 k_j\Delta t}, \qquad \widehat{\boldsymbol{\beta}}_{j,\{n\}} = \left(\widehat{\boldsymbol{b}}_{j,\{n\}}^{(0)} + \widehat{\boldsymbol{b}}_{j,\{n\}}^{(1)}\right) e^{in\boldsymbol{\sigma}_1 k_j\Delta t}, \qquad (37)$$

where the quantities with superscript '(0)' vary slowly in time and those with superscript '(1)' are small. Note, however, that the time dependence explicitly stated in (37) is different from that in (21). In the latter case, since the perturbation $\widetilde{\boldsymbol{\psi}}(x)$ was spectrally localized near some wavenumber k_0, it was appropriate to assume that in the main order, all harmonics evolved proportionally to the same factor, either $\exp[-in\boldsymbol{\sigma}_1 k_0\Delta t]$ or $\exp[in\boldsymbol{\sigma}_1 k_0\Delta t]$. On the other hand, since the perturbation (35), considered in this section, is *not* spectrally localized, then the principal evolution of each Fourier harmonic followed its individual exponential, $\exp[\mp in\boldsymbol{\sigma}_1 k_j\Delta t]$. A consequence of this difference will appear in the subsequent derivation.

When one substitutes (37) into (36), one obtains, similarly to (22), two distinct groups of oscillating terms. For example, the $\widehat{\boldsymbol{P}}_l\widehat{\boldsymbol{\alpha}}_{j-l,\,\{n\}}$ term yields:

$$e^{in\boldsymbol{\sigma}_1 k_j n\Delta t}\,\widehat{\boldsymbol{P}}_l\,\widehat{\boldsymbol{\alpha}}_{j-l,\,\{n\}} = \left(\widehat{\boldsymbol{P}_{01}}_l\,e^{in\boldsymbol{\sigma}_1 k_l n\Delta t} + \widehat{\boldsymbol{P}_{23}}_l\,e^{in\boldsymbol{\sigma}_1(k_l-2k_j)n\Delta t}\right)\left(\widehat{\boldsymbol{a}}_{j-l,\,\{n\}}^{(0)} + \widehat{\boldsymbol{a}}_{j-l,\,\{n\}}^{(1)}\right). \qquad (38)$$

The terms in the first group on the r.h.s. vary on the time scale of order $O(1)$ (see the second sentence after (36)), while the terms in the second group vary much faster due to the first inequality in (35b).[1] Then, arguing as in the paragraph surrounding Eqs. (24), one shows that the rapidly oscillating terms affect only the small corrections $\widehat{\boldsymbol{a}}_{j,\{n\}}^{(1)}$, $\widehat{\boldsymbol{b}}_{j,\{n\}}^{(1)}$, but in the main order do not contribute to the evolution of the principal terms $\widehat{\boldsymbol{a}}_{j,\{n\}}^{(0)}$, $\widehat{\boldsymbol{b}}_{j,\{n\}}^{(0)}$. Therefore, in what follows we omit those rapidly oscillating terms and will also omit the superscript (0), as done after (25). Following the above steps

---

[1] Note that since we intend to investigate an unconditional numerical instability, one can consider the limit $\Delta t \to 0$, and thus there can be no resonances like (14), because of which any of the terms from the second group may become slowly varying.

and also approximating the finite differences in time with time derivatives, as done in obtaining (31) from (30), we find:

$$(\widehat{\boldsymbol{a}}_j)_t = i\Omega\widehat{\boldsymbol{a}}_j + \frac{i}{N}\sum_l \widehat{\boldsymbol{P}_{01}}_{\,l}\, e^{i\boldsymbol{\sigma}_1 k_l t}\,\widehat{\boldsymbol{a}}_{j-l} + \widehat{\boldsymbol{Q}_{01}}_{\,l}\, e^{i\boldsymbol{\sigma}_1 k_l t}\,(\widehat{\boldsymbol{b}}_{j-l})^*\,, \tag{39a}$$

$$(\widehat{\boldsymbol{b}}_j)_t^* = -i\Omega(\widehat{\boldsymbol{b}}_j)^* - \frac{i}{N}\sum_l \widehat{\boldsymbol{Q}_{01}}_{\,l}^{\,*}\, e^{-i\boldsymbol{\sigma}_1 k_l t}\,\widehat{\boldsymbol{a}}_{j+l} + \widehat{\boldsymbol{P}_{01}}_{\,l}^{\,*}\, e^{-i\boldsymbol{\sigma}_1 k_l t}\,(\widehat{\boldsymbol{b}}_{j+l})^*\,, \tag{39b}$$

where $t \equiv n\Delta t$.

Exact solution of system (39) would be possible only by direct numerical simulations. Not only would such an approach not be illuminating in any respect, but it would also be considerably more difficult than solving (31) (or, equivalently, (34)), despite the latter equation appearing to have more terms. Indeed, (39), unlike (31), has time-dependent terms on the r.h.s., which is the consequence of the difference between (37) and (21), emphasized after (37). Even more importantly, the system in (39) couples, by virtue of (35b), a much greater number of Fourier harmonics, $\lesssim N/2$ instead of $M \ll N/2$. For these reasons, below we will use a *simplified approach*. It will still require a numerical solution, but only of a 2×2 system. More importantly, it will allow us to *explain the mechanism* by which harmonics of the "noise floor" can become unstable.

The simplification occurs from an observation that none of the coefficients of terms $\widehat{\boldsymbol{a}}$ and $\widehat{\boldsymbol{b}}$ on the r.h.s. of (39) depends on the harmonic's index j. Therefore, these equations will be satisfied by a j-independent ansatz:

$$\widehat{\boldsymbol{a}}_j \equiv \widehat{\boldsymbol{a}}, \qquad \widehat{\boldsymbol{a}}_j \equiv \widehat{\boldsymbol{b}} \qquad \text{for all } j \text{ satisfying (35b).} \tag{40}$$

We will come back to interpretation of this ansatz later in this Section. We now expand $\widehat{\boldsymbol{a}}$ and $\widehat{\boldsymbol{b}}$ using (32), substitute the result into (39) and collect the scalar coefficients of vectors $\boldsymbol{e}_{(\pm)}$. For example, the coefficients at $\boldsymbol{e}_{(+)}$ yield:

$$(\widehat{a}_{(+)})_t = i\Omega\widehat{a}_{(+)} + \frac{i}{N}\sum_l \widehat{P_0}_{\,l}\, e^{ik_l t}\,\widehat{a}_{(+)} + \left(\widehat{Q_0}_{\,l} + \widehat{Q_1}_{\,l}\right) e^{ik_l t}\,(\widehat{b}_{(+)})^*\,, \tag{41a}$$

$$(\widehat{b}_{(+)})_t^* = -i\Omega(\widehat{b}_{(+)})^* - \frac{i}{N}\sum_l \left(\widehat{Q_0}_{\,l}^{\,*} + \widehat{Q_1}_{\,l}^{\,*}\right) e^{-ik_l t}\,\widehat{a}_{(+)} + \widehat{P_0}_{\,l}^{\,*}\, e^{-ik_l t}\,(\widehat{b}_{(+)})^*\,, \tag{41b}$$

where we have used that $P_1 \equiv 0$. In deriving (41) we have also used the first two of identities (33) as well as the identity

$$e^{i\boldsymbol{\sigma}_1 k_l t}\, \boldsymbol{e}_{(\pm)} = e^{\pm ik_l t}\, \boldsymbol{e}_{(\pm)}\,, \tag{42}$$

which follows from (19) and (33). Note that unlike in (34), terms $\widehat{a}_{(+)}, \widehat{b}_{(+)}$ are not coupled with $\widehat{a}_{(-)}, \widehat{b}_{(-)}$ due to the absence of matrices $\boldsymbol{\sigma}_2$, $\boldsymbol{\sigma}_3$ in (39).

Here comes the next *key step* in this analysis: we recognize the sums in (41) as the inverse Fourier transform (16) (but in t, not in x), upon which we rewrite Eqs. (41) and their counterparts obtained for $\widehat{a}_{(-)}, \widehat{b}_{(-)}$ as:

$$(\boldsymbol{c}_{(\pm)})_t = \boldsymbol{R}_{(\pm)}\, \boldsymbol{c}_{(\pm)}, \tag{43a}$$

where:

$$\boldsymbol{c}_{(\pm)} = \begin{pmatrix} \widehat{a}_{(\pm)} \\ (\widehat{b}_{(\pm)})^* \end{pmatrix}, \qquad \boldsymbol{R}_{(\pm)} = i\boldsymbol{\sigma}_3 \left(\Omega\boldsymbol{\sigma}_0 + \begin{pmatrix} P_0(\pm t) & Q_0(\pm t) \pm Q_1(\pm t) \\ Q_0^*(\pm t) \pm Q_1^*(\pm t) & P_0^*(\pm t) \end{pmatrix} \right).$$
(43b)

Two remarks about the entries of the last matrix in (43b) are in order, both of which are consequence of the difference emphasized after Eqs. (37). First, while P_0 etc. were defined in (11) as functions of x, in the above system they are functions of time. Second, due to the periodicity of discrete Fourier transform, these entries are *periodic*, with the period being L, the length of the computational domain. Thus, although in (43a), $t \in [0, \infty)$, one also requires that

$$P_0(t + L) = P_0(t), \qquad Q_{0,1}(t + L) = Q_{0,1}(t) \qquad \forall\, t.$$
(43c)

Before we discuss the solution of (43), let us point out that we need to solve *only one*, not two, systems. This follows from the parity properties implied by (11) and (8):

$$P_0(-t) = P_0(t), \qquad Q_0(-t) = Q_0(t), \qquad Q_1(-t) = -Q_1(t),$$
(44)

whence $\boldsymbol{R}_{(-)} = \boldsymbol{R}_{(+)}$. Therefore, below we will omit the subscripts '$(\pm)$' of $\boldsymbol{c}$ and $\boldsymbol{R}$. As yet another simplification, we note that $P_0^* = P_0$, $Q_0^* = Q_0$, while $Q_1^* = -Q_1$. Finally, using the explicit form of P_0, Q_0, Q_1, we can rewrite (43) as:

$$\boldsymbol{c}_t = i\boldsymbol{\sigma}_3 \left(\Omega\boldsymbol{\sigma}_0 + \frac{1}{2} \begin{pmatrix} \Psi_1^2 - \Psi_2^2 & (\Psi_1 + \Psi_2)^2 \\ (\Psi_1 - \Psi_2)^2 & \Psi_1^2 - \Psi_2^2 \end{pmatrix} \right) \boldsymbol{c}.$$
(45)

Recall that here, $\Psi_{1,2}$ are L-periodic functions of time. Then,

$$\|\boldsymbol{c}(t)\| \le \|\boldsymbol{\Phi}(L)\|^{t/L} \|\boldsymbol{c}(0)\|, \qquad t = \text{integer} \cdot L,$$
(46a)

where the fundamental solution $\Phi(L)$ of (45) satisfies

$$\boldsymbol{c}(L) = \boldsymbol{\Phi}(L)\, \boldsymbol{c}(0),$$
(46b)

and $\| \cdots \|$ denotes the 2-norm.

We are now ready to interpret the meaning of ansatz (40). A perturbation (35) where amplitudes of the harmonics satisfy (40) is approximately[2] the sum of *two* delta functions in space, where the 'two' occurs due to (32) having two contributions, from $\boldsymbol{e}_{(+)}$ and $\boldsymbol{e}_{(-)}$. By virtue of (37), these two spikes move with speed 1 in opposite directions. Due to the periodicity of the boundary conditions, they repeatedly leave and re-enter the computational domain. Their amplitudes are changed when they pass through the soliton and remain constant far from the soliton; this follows from (45). If those amplitude changes from consecutive passages are accumulated, the amplitude of the "noise floor" increases; see the dashed line in Fig. 6(b) and Fig. 10, which will be described in detail below.

_____

[2]This would have been exact if the summation had extended for all $j \in [1, N/2]$.

When the initial "noise floor" consists of white noise as opposed to the simplified ansatz (40), the above interpretation no longer applies in the exact sense. However, the mechanism of the instability of the "noise floor" is the same: the perturbation (35) repeatedly passes through the soliton, and when changes of its amplitude over consecutive passages accumulate, the perturbation's amplitude grows on average exponentially. The fact that the evolution of the "simplified" perturbation (35), (40) is predictive of that of the generic perturbation is seen in Figs. 6 and 10.
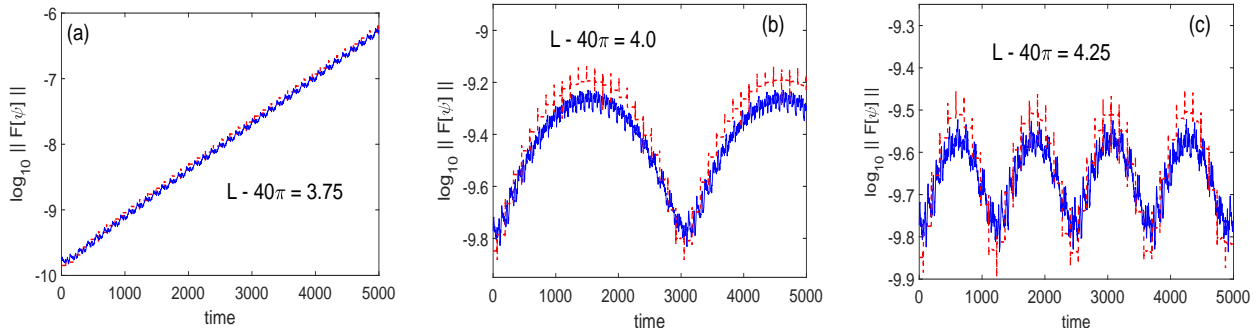
Figure 10: Evolution of the amplitude of harmonics of the "noise floor", similar to that shown in Fig. 6(b), but for $\Omega = 0.50$ and the three values of L indicated in the panels. Solid and dashed lines correspond to a small white noise or a constant, respectively, being added to each Fourier mode in the initial condition.

Let us point out a difference between the long-time evolution of the "noise floor" and that of the modes at the edge of the spectral domain, considered in Section 5. The long-term behavior (growth or absence of such) in both these cases is determined, of course, by the spectral radius ρ of the corresponding fundamental solution ($\Phi(L)$ in the case of (45)). However, in the case of the "noise floor", the norm of $\Phi(L)$ also plays a certain role. Given the well-known relation between the two (see, e.g., [28]):

$$\rho(\mathbf{\Phi}(L)) \leq \|\mathbf{\Phi}(L)\| = \sigma_{\max}(\mathbf{\Phi}(L)), \tag{47}$$

where $\sigma_{\max}$ is the maximum singular value, one can see that the norm determines the *transient* behavior of the "floor", occurring for t/L being a relatively small integer (see below). Given that values $L \sim 100$ are typical in simulations of the Gross–Neveu soliton, such "transient" behavior is what may be observed in simulations of the soliton dynamics over several hundreds of time units. This is shown in Fig. 10, where the periodic oscillations of the magnitude of the "floor" harmonics occur because they may grow for a few passages through the soliton (see the previous paragraph) due to $\|\mathbf{\Phi}(L)\| > 1$, but then periodically return to their initial values if $\rho(\mathbf{\Phi}(L)) = 1$.

In Fig. 11 we plot the growth rate of the "noise floor" versus L. The theoretical values are inferred from the spectral radius of $\mathbf{\Phi}(L)$, which was found by the above analysis, via the relation (see (46a)):

$$\text{growth rate} = \big(\ln \rho(\mathbf{\Phi}(L)) \big)/L. \tag{48}$$

The numerical values were found by direct numerical simulation of the Gross–Neveu soliton by the SSM, via measuring the amplitude of the Fourier harmonic at $k = k_{\max}/2$ and following the

24

procedure similar to that described at the end of Section 5. The agreement between our analysis and direct numerics is seen to be quite good.
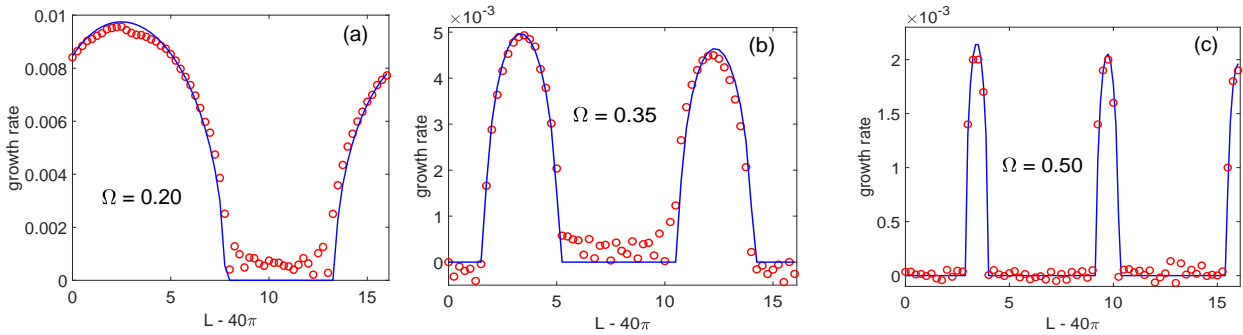

Figure 11: Growth rate of the "noise floor" as the function of length L of the computational domain for the same three values of Ω as in Fig. 8. Note different vertical scales in the three panels. Solid lines correspond to the analytical solution of (45), as explained in the text, while circles are the result of direct numerical simulation with the SSM. The simulation times for panels (b) and (c) are the same as the corresponding times in Figs. 7(b,c) and 8(b,c): $t = 1500$ and $t = 5000$. For panel (a), the simulation time is $t = 1000$. This larger time than in Figs. 7(a) and 8(a) had to be used to decrease the effect of the transient behavior (see Figs. 10(b,c)) on the computed growth rate (see text). Moreover, since for $\Omega = 0.2$, the NI at $k \approx \pm k_{\max}$ is so strong that it would destroy the numerical solution at $t = 1000$ (see Fig. 8(a)), we had to filter out harmonics near the edges of the computational spectral domain.

Three remarks related to Fig. 11 are in order. First, small discrepancies between the analytical and numerical solution in those regions where the growth rate vanishes is the numerical artifact. It occurred because for the corresponding values of L, the "floor" harmonics may exhibit periodic evolution, as shown in Fig. 10(b,c). Then, the harmonic's amplitude at $t = t_{\max}$ may differ from that at $t = 0$, even though *on average* the harmonic does not grow. The fact that the discrepancy decreases with Ω is due to the fact that we used larger $t_{\max}$ for larger Ω, so that the error in the growth rate, which was obtained by the "rise over run" formula, was decreased for the larger "run" (i.e., $t_{\max}$). Second, the dependence of $\rho(\mathbf{\Phi}(L))$ on L is *exactly* periodic; see next paragraph and Appendix E. The slight decrease in the magnitude of the peaks of the growth rate, seen in Figs. 11(b,c) is due to the presence of L in the denominator of (48). Third, while the spectral radius of $\mathbf{\Phi}(L)$ varies with with L, the norm of $\mathbf{\Phi}(L)$ does not; it equals the maximum value of the spectral radius, in accordance with (47). The independence of $\|\mathbf{\Phi}(L)\|$ on L is explained in Appendix E.

The numerical solution of system (45) leaves it unclear why $\rho(\mathbf{\Phi}(L))$ depends on L. Moreover, such a dependence may even seem counter-intuitive given that the amplitude of the perturbation (35) changes only in the vicinity of the soliton (which does not depend on L) and remains intact in the rest of the computational domain. A qualitative resolution to this conundrum comes from the observation that while the eigenvalues of matrix $\mathbf{R}$ in (43) (or, equivalently, (45)) are imaginary (for each given t), $\mathbf{R}/i$ is not Hermitian, and therefore the evolution that it defines is not unitary (i.e.,

25

the solution's norm is not preserved). In Appendix E we present a more quantitative argument to that effect. It explains the origin of the periodic dependence of $\rho(\mathbf{\Phi}(L))$ on L, with the period being $2\pi/(2\Omega)$, while showing that, at the same time, $\|\mathbf{\Phi}(L)\|$ does not depend on L.

To conclude this section, we note that while the "noise floor" NI decreases when Ω increases, it is still present even for solitons with $\Omega = 0.75$. In Fig. 9(b) we show the growth rate versus L for this value of Ω. The results numerical and analytical for the "noise floor" NI agree well. However, we also observed a new feature of the NI, which we never observed in simulations for $\Omega \leq 0.5$; this feature is responsible for the results shown in Fig. 9(b) with stars. This new type of NI bifurcates from the "noise floor" NI but eventually develops a spectral shape that is distinctly different from the flat "noise floor" profile. We discuss the corresponding details in Appendix F, where we also mention a possible extension of the analysis of this section that may be able to explain some of its features. However, we do not carry out such an analysis for a number of reasons. First, we did not observe this NI for $\Omega \leq 0.5$, which means that it can affect the solution of the Gross–Neveu model only in ultra-long simulations, with time well in excess of $t = 10,000$. Second, our proposed extension would apply only for a short range of L values where this NI is spectrally broad. When it becomes spectrally localized, a combination of that extension and the analysis of Section 4 may become needed. Thus, developing such an analysis would noticeably increase the already large size of this paper, while potentially providing an explanation for a phenomenon that can possibly be observed only in exceptionally long simulations.

7   Generalizations

Here we will show that the two types of NI considered in Sections 5 and 6 occur in more general situations than in simulations of a single Gross–Neveu soliton. Thus, these types of NI appear to be engendered not by a specific model, its solution, or even the numerical method, but by a combination of various factors. Namely, we will first show that the same phenomena occur for more general solutions of the same model. Second, we will show that one of them occurs for the soliton of a different, well-known model in the relativistic field theory. Third, we will explain why, and show that, the same types of NI occur in other popular numerical methods applied to the Gross–Neveu model. Finally, we will show that by changing the boundary conditions of the numerical method, one can strongly diminish both types of NI.

7.1   More general solutions of the Gross–Neveu model

In Fig. 12 we show the result of simulation of two colliding solitons (9). The parameters of the solitons are: $\Omega_1 = 0.25$, $V_1 = 0$, $(x_0)_1 = 0$; $\Omega_2 = 0.15$, $V_2 = 0.1$, $(x_0)_2 = -8\pi$. The relative velocity of the solitons was chosen sufficiently small so that the solution would differ from two separated solitons for a relatively long time. The simulation parameters are: $L = 160\pi$, $N = 2^{14}$, $\Delta t = \Delta x/5$, where the computational domain was chosen to be larger than that in the rest of this paper to minimize the effect of radiation re-entering the domain and possibly corrupting the solution. The

NI at the edges of the spectral domain is clearly visible. Moreover, one can see that the spectral support of unstable modes greatly expands between $t = 175$ and $t = 200$, which is when the moving soliton comes in close proximity with the standing one.
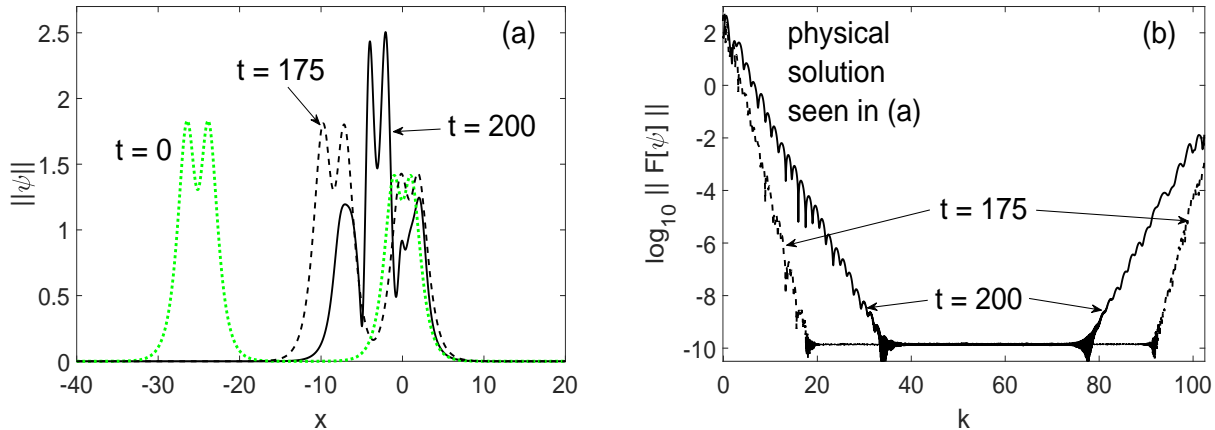

Figure 12: Colliding solitons described in Section 7.1. Panel (a): Dotted (green), dashed, and solid lines correspond to the solution at $t = 0$, 175, and 200. Only part of the computational domain is shown for better visibility. Panel (b): Spectra (for $k \geq 0$) of the numerical solution at $t = 175$ (dashed) and $t = 200$ (solid).

We also considered the evolution of an initial pulse both of whose components are 20% greater than the standing soliton (8) with $\Omega = 0.2$. The NI at the edges of the computational domain destroys this solution by $t \gtrsim 300$. (It should be noted that some other combinations of the components of the initial pulse, — e.g., where one is 20% greater and the other is 20% smaller than those of the soliton, — do *not* lead to a strong NI. This occurs because such an initial pulse evolves towards a soliton with a greater value of Ω, for which the NI is considerably weaker.)

7.2 Numerical instability for the Massive Thirring soliton

The Massive Thirring model in laboratory coordinates:

$$u_t + u_x = i(v + u|v|^2), \qquad v_t - v_x = i(u + v|u|^2), \tag{49}$$

has the one-soliton solution [26, 29, 30] which, for zero velocity, can be written as:

$$U_{\text{sol}} = \frac{\sin Q \, \exp[-it \cos Q]}{\cosh(x \sin Q - iQ/2)}, \qquad V_{\text{sol}} = \frac{-\sin Q \, \exp[-it \cos Q]}{\cosh(x \sin Q + iQ/2)}, \qquad Q \in [0, \pi]. \tag{50}$$

It may be noted that the Gross–Neveu and Massive Thirring models both belong to the more general class of fermionic (nonlinear Dirac) field-theoretic models, corresponding to the cases of scalar–scalar and vector–vector interactions, respectively [26]. The Massive Thirring model is integrable by the Inverse Scattering Transform [31, 32], a consequence of which is that the soliton solution (50) is physically stable. Incidentally, a model similar to (49) occurs in a different field — that of nonlinear light propagation in optical fibers with a periodic refractive index [34]. However, its soliton (known as the gap soliton) is physically unstable in a certain range of its parameters

[35]. Therefore, we chose to consider only the stable soliton (50) of model (50) to avoid any issue of possible coexistence of physical and numerical instabilities.

To apply the SSM to (49), one first solves the linear part of those equations in the Fourier domain:

$$\begin{pmatrix} \widehat{u} \\ \widehat{v} \end{pmatrix}_{\text{lin}} = \frac{1}{1+\delta^2} \begin{pmatrix} e^{i\gamma\Delta t} + \delta^2 e^{-i\gamma\Delta t} & \delta\left(e^{i\gamma\Delta t} - e^{-i\gamma\Delta t}\right) \\ \delta\left(e^{i\gamma\Delta t} - e^{-i\gamma\Delta t}\right) & \delta^2 e^{i\gamma\Delta t} + e^{-i\gamma\Delta t} \end{pmatrix} \begin{pmatrix} \widehat{u} \\ \widehat{v} \end{pmatrix}_n, \tag{51a}$$

where $\gamma = \sqrt{k^2+1}$, $\delta = k + \gamma$. Then the nonlinear substep is:

$$\begin{pmatrix} \widehat{u} \\ \widehat{v} \end{pmatrix}_{n+1} = \begin{pmatrix} u_{\text{lin}} \exp[i|v_{\text{lin}}|^2 \Delta t] \\ v_{\text{lin}} \exp[i|u_{\text{lin}}|^2 \Delta t] \end{pmatrix}. \tag{51b}$$

Using the SSM (51) to simulate (49) with the initial condition consisting of the soliton (50) with $Q = 0.35\pi$ and white noise of magnitude on the order of 10^{-12}, we have observed the numerically unstable modes at the edges of the spectrum grew by 7 orders of magnitude in $t = 1000$. The simulation parameters were: $L = 40\pi$, $N = 2^{12}$, and $\Delta t = \Delta x/5$. The spectrum of the numerical solution looks qualitatively similar to that shown in Fig. 4(a) and therefore is not shown here. For greater Q, this NI developed even faster.[3] Conversely, for smaller Q, we found that this NI decreases. For example, for $Q = 0.30\pi$ we found that the unstable modes at the spectral edges grow at most by two orders of magnitude when we performed this simulation for a variety of values of L.

We were unable to observe the "noise floor" NI for the Massive Thirring soliton in our numerics for any values of Q and L and initially were surprised. However, an analysis similar to that presented in Section 5 revealed that for this model, this type of NI does not occur. Below we present a summary of this analysis. Although it is possible to apply it directly to Eqs. (49), it is more convenient to cast those equation in a form with the l.h.s. identical to that of the Gross–Neveu model (2) so as to follow the analysis of Section 6 as closely as possible. To that end, defining

$$\psi_1 = (u+v)/\sqrt{2}, \qquad \psi_2 = (u-v)/\sqrt{2}, \tag{52}$$

we transform (49) into

$$\psi_{1,t} + \psi_{2,x} = \frac{1}{2}\left(\psi_1|\psi_1|^2 - \psi_1^*\psi_2^2\right) + i\psi_1, \tag{53a}$$

$$\psi_{2,t} + \psi_{1,x} = \frac{1}{2}\left(\psi_2|\psi_2|^2 - \psi_2^*\psi_1^2\right) - i\psi_2, \tag{53b}$$

Linearizing (53), we obtain equations of the form (11a) with Ω on the l.h.s. being replaced by $\cos Q$ and with:

$$P_0 = \frac{1}{2}\left(|\Psi_1|^2 + |\Psi_2|^2\right), \qquad P_1 = -\text{Re}\left(\Psi_1\Psi_2^*\right), \qquad Q_0 \equiv 0, \qquad Q_1 \equiv 0, \tag{54a}$$

$$P_2 = -\text{Im}\left(\Psi_1\Psi_2^*\right), \qquad P_3 = \frac{1}{2}\left(|\Psi_1|^2 - |\Psi_2|^2\right) + 1, \qquad Q_2 \equiv 0, \qquad Q_3 = \frac{1}{2}\left(\Psi_1^2 - \Psi_2^2\right), \tag{54b}$$

---

[3]The limit $Q \to \pi$ for the Massive Thirring soliton is known to be similar to the limit $\Omega \to 0$ for the Gross–Neveu soliton.

where $\Psi_{1,2}$ are the exact one-soliton solutions obtained from (50) and (52). Moreover, using the specific form of the soliton (50), one further finds that

$$P_1 \equiv 0. \tag{54c}$$

The information about the possible growth of the "noise floor" perturbation is found from Eqs. (43a), where the matrix on the r.h.s. is now:

$$\boldsymbol{R}_{(\pm)} \ = \ i\boldsymbol{\sigma}_3 \left(\cos Q\boldsymbol{\sigma}_0 + \begin{pmatrix} P_0(t) & 0 \\ 0 & P_0(t) \end{pmatrix} \right), \tag{55}$$

where we have used that P_0 is a real-valued and even function. The key point to note is that due to the absence of off-diagonal terms in (55), the evolution of the perturbation $\boldsymbol{c}$ is unitary, and hence there is no "noise floor" NI in this case.

7.3 Numerical instability of other methods applied to Gross–Neveu soliton

In our analysis of the NI in Sections 5 and 6 there was nothing that would explicitly refer to the SSM as opposed to any other numerical method. Indeed, all we did was obtain a differential (in time) equation for the error in the limit $\Delta t \to 0$. There was, however, an *implicit* assumption: that the numerical scheme does not change the linear dispersion relation (5) (for $|k| \gg 1$). Therefore, we expect that similar NI should occur for any other numerical scheme that preserves the linear dispersion relation of models (2) and (49).

One such family of schemes are the Exponential Time Differencing (ETD) and Integrating Factor methods (see, e.g., [36]). It should be noted that for the Gross–Neveu model, such methods were first proposed in [37]. We implemented the ETD method based on the 4th-order explicit Runge–Kutta (RK) solver, referred to as ETD4RK in [36] and given by Eqs. (26)–(29) in that paper. For the implementation of the ETD methods, it is convenient to rewrite the simulated equation in a form where the matrix multiplying the spatial derivative terms is diagonal. For Eqs. (2) this is achieved via the transformation inverse to (52), upon which they take on the form:

$$u_t = -u_x + i(u|v|^2 + u^*v^2 - v), \qquad v_t = \ v_x + i(v|u|^2 + v^*u^2 - u) \,. \tag{56}$$

In simulating the Gross–Neveu equations in this form with the ETD4RK, we observed both types of NI — at the spectral edges and of the "noise floor", — with their growth rates being practically the same (for the selected values of L that we tested) to those reported in Sections 5 and 6, as long as $\Delta t < \Delta x$ (see (6)).

The other method for which we tested the presence of NI in the Gross–Neveu model is the pseudo-spectral 4th-order RK method. To implement it, one solves Eqs. (56) (or (2)) by the classical RK method in time, with the spatial derivatives being computed by the direct and inverse Fourier transform (16). This method preserves the dispersion relation (5) *only* in the limit $k_{\max}\Delta t \equiv (\pi/\Delta x)\Delta t \ll 1$, where the 4th-degree polynomial in $\Delta t k$, which results from the 4th-order RK method, approximates $\exp[ik\Delta t]$ sufficiently closely for all wavenumbers. However, recall that

we are interested in demonstrating the *unconditional* NI, which persists in the limit $\Delta t \to 0$. Therefore, at least for sufficiently small Δt, the NI in the pseudo-spectral method is expected to develop similarly to that in the SSM. We confirmed this to indeed be the case. For example, for $\Omega = 0.2$, the NI at the spectral edge was suppressed by the numerical diffusion of the pseudo-spectral method for $\Delta t = \Delta x/5$; however, for $\Delta t = \Delta x/10$, the numerical diffusion became weak enough to allow this NI to develop almost as fast as in the SSM. For $\Omega = 0.1$, even the relatively strong numerical diffusion was not able to prevent the NI at the spectral edge from destroying the numerical solution around $t = 200$. Also, the "noise floor" NI in the pseudo-spectral method was similar to that in the SSM for both $\Delta t = \Delta x/5$ and $\Delta t = \Delta x/10$.

Finally, it is appropriate to mention that we also observed both types of NI when simulating Eqs. (56) with various "flavors" of the Method of Characteristics (MoC). The "flavor" of the MoC is determined by the specific ordinary differential equation solver that is used along the characteristics. We used periodic boundary conditions, to be consistent with those imposed by the Fourier SSM and the two methods described in this subsection. However, condition $\Delta t = \Delta x$ is required as an essential part of the MoC, and this modifies the dynamics of modes at the spectral edge (where then $k_{\max} = k_{\pi}$; see (14)). The development of the NI at the spectral edge then appears to depend on which "flavor" of the MoC is used, and a detailed analysis of this issue falls outside the scope of this paper. However, the "noise floor" NI was observed, and was similar, for all "flavors" of the MoC that we used to simulate the Gross–Neveu soliton.

7.4   Suppression of the numerical instability for the Gross–Neveu soliton

The previous subsection illustrated the fact that the appearance of NI in simulations of the Gross–Neveu soliton with sufficiently small Ω occurs not just for the Fourier SSM, but for a variety of numerical methods. In fact, NI for this problem was earlier reported in [23, 24], although no details about its nature were investigated in those studies. On the other hand, we showed in [25] that merely imposing *nonreflecting* boundary conditions (BC) allows the small-Ω soliton to survive over several thousands of time units. Consequently, we inferred that the soliton can eventually be destroyed by the radiation re-entering the computational domain. However, in [25], we did not specify the spectral content of such radiation and whether or not harmonics generated by either types of the NI considered in this work contribute to the destruction of the soliton. We will briefly address these questions below.

First, let us clarify that nonreflecting BC in the linear substep of the non-Fourier SSM are imposed for the variables defined in (52):

$$u(-L/2) = 0, \qquad v(L/2) = 0. \tag{57}$$

In the absence of the terms on the r.h.s. of (56) other than u_x and v_x, these BC lead to any initial perturbation completely (i.e., without reflection) leaving the computational domain upon reaching the boundaries. *With* the other terms, this "leaving" is incomplete, but the reflection diminishes

as the wavenumber increases, since for higher Fourier harmonics, the terms u_x and v_x become increasingly dominant. Therefore, we conclude that the dynamics of harmonics with $|k| \gg 1$, which is where both types of the unconditional NI were found in this paper, will be determined by the balance between, on one hand, the loss due to the perturbation leaving the computational domain and, on the other, either of the growth mechanisms described in Sections 5 and 6.

We verified that for $\Omega = 0.2$ and the simulation parameters $L = 40\pi$, $N = 2^{12}$, and $\Delta t = \Delta x$,[4] neither type of NI was observed in the simulations up to $t = 5000$. However, for $\Omega = 0.1$, the spectral edge NI was indeed observed, and the corresponding modes grew by some 8 orders of magnitude over the same time (see next paragraph). In contrast, the harmonics of the "noise floor" grew by less than two orders of magnitude. This is consistent with our observations that both types of NI become stronger as Ω decreases, and that between the two types, the spectral edge NI is significantly stronger.

Whether it will be this NI that eventually destroys the soliton simulated with the nonreflecting BC, depends on the simulation parameters. We observed that for the $\Omega = 0.1$-case described in the previous paragraph, the soliton was destroyed by *low-k* radiation before $t = 4000$. This is in line with the statement made after (57), according to which low-k harmonics experience more refection back into the computational domain and hence are attenuated less by the BC (57). (Also, we remind the reader that the reason why the soliton becomes more "fragile" for smaller values of Ω remains an open problem.) Therefore, in order for the soliton not to be visibly affected by the low-k radiation, we had to use more grid points ($N = 2^{15}$): this reduces the discretization error, which is the source of such radiation. *However*, there is a limit to how much one can "prolong the soliton's life" by further increasing N, and this limit is set by the spectral edge NI. This NI does not depend on how fine the computational grid, and how small the time step, are and hence eventually will cause the highest-k harmonics destroy the soliton, if low-k ones have not done so already. The only way to circumvent this, to the best of our knowledge, is to impose additional absorbing boundary conditions, as demonstrated in [25].

8 Conclusions

In this work, we showed that the Fourier SSM, (13) or (15), for the Gross–Neveu model (2) may exhibit three types of NI. The first type, analyzed in Section 4, *may* occur when the time step exceeds the "threshold" (6) set by the Courant–Friedrichs–Lewy condition. However, unlike in other schemes for hyperbolic equations, this NI of the SSM can be observed *only* if the simulated solution of the model exhibits *physical* (i.e., not numerical) instability. For reasons explained in Section 2, we refer to such a solution as "fragile" rather than unstable. Thus, one can simulate non-fragile solutions of Eqs. (2) with Δt that significantly exceeds the "threshold" (6) and not observe any instability for very long simulation times ($t = O(10,000)$). The qualitative reason

---

[4]This is dictated by the fact that the linear substep of the SSM is performed by the MoC without interpolation between nodes; see [25]. Also, see the note at the end of the previous subsection regarding condition $\Delta t = \Delta x$.

behind this is that the Fourier modes near the resonant wavenumbers (14), where this type of NI can occur, satisfy the same equations — the linearized Gross–Neveu model (11) — as the "physical" perturbations with the wavenumbers of order one.

The NI of the second type, analyzed in Section 5, occurs near the edges of the computational spectrum. It is *unconditional*, i.e. persists for arbitrarily small Δt. This type of NI becomes stronger as Ω of the soliton decreases, i.e., as the soliton becomes more "fragile". While the corresponding growth rate depends on the length L of the computational domain, this dependence diminishes as Ω decreases: see Figs. 8 and 9(a). There is no "simple" qualitative reason that would unambiguously explain the origin of this NI. However, one can easily see that the (in)stability of the highest-k harmonics is *not* related to the that of a "physical" (i.e., low-k) perturbation, because the two groups of perturbations satisfy *different* equations: (C.2) ($|k| \lesssim k_{\max}$) and (11) ($|k| = O(1)$). Our analysis of this NI did require a numerical solution of a relatively large eigenvalue problem, but this is still several orders of magnitude faster than direct numerical simulations, especially for non-fragile solitons.

The NI of the third type, analyzed in Section 6, occurs for Fourier harmonics of the "noise floor", defined as having wavenumbers much greater than those where most of the soliton's energy is found, yet sufficiently far from the spectral edge: see (35b). This type of NI is also unconditional, and it also becomes stronger as Ω of the soliton decreases. The growth rate is essentially periodic in L, but also decreases in inverse proportion to it (i.e., for a sufficiently large L, slowly). Unlike for the second type of NI, there *is* a qualitative explanation for the third one. Namely, it can occur as perturbations travelling in the opposite directions interact in the vicinity of the soliton. This process can be amplified when the perturbations do so repeatedly, which is enabled by their staying in the computational domain due to periodic boundary conditions. Then, it is indeed natural that the growth rate of these perturbations is inversely proportional to the time interval over which they experience repeated interaction. This time interval is proportional to the length of the computational domain. Finally, we note that: (i) analysis of this NI requires numerical solution of only two coupled ordinary differential equations; see Eqs. (43) and (45); and (ii) this analysis was able to explain the *absence* of the "noise floor" NI in the Massive Thirring model (Section 7.2).

In addition to revealing and analyzing these three types of NI, the latter two of which have not been reported in previous studies of the SSM,[5] we also demonstrated, in Section 7, that they can occur in more general situations. First, they occur in multi-soliton solutions, as long as some of the consitituent solitons have a sufficiently small Ω. In fact, these NIs appear to be amplified during the collision of two solitons. Second, they can occur for other models that involve solitons in dispersionless coupled-mode equations; an example is the Massive Thirring soliton. Third, they can occur for methods other than the SSM.

Based on these generalizations, we propose that there may be only two essential conditions that

---

[5]We only briefly mentioned them in an Appendix of [25], but did not provide any analysis.

need to be met for these NIs to be observed. The first is the boundary conditions that permit a substantial part of the radiation that has reached a boundary, to re-enter the computational domain. The simplest such boundary conditions are periodic; they are automatically imposed when the numerical method involves the discrete Fourier transform. However, there are indications in [24] that other boundary conditions, such as homogeneous Dirichlet, may also lead to similar NIs. On the other hand, nonreflecting boundary conditions were shown (see Section 7.4) to suppress these NIs considerably stronger.

The second essential condition for observing these NIs is that the simulated soliton's parameters must be in a certain range (e.g., a sufficiently small Ω for the Gross–Neveu soliton or a sufficiently large Q for the Massive Thirring soliton). Although the NI at the spectral edge, and to a lesser extent the "noise floor" NI, were found even for Gross–Neveu solitons with Ω as large as 0.75, their growth rate was quite small, and hence they may not be observed in any but the ultra-long-time simulations. Thus, an essential overall conclusion of this study is that stability of numerical methods for nonlinear evolution equations depends not only on the method itself or the equation to which it is applied, but also on the parameters of the background solution which is being simulated. Earlier this was demonstrated for the NLS soliton [38], where merely changing the soliton's speed would significantly affect the observed NI.

Finally, we would like to mention three different groups of physical models, in numerical simulations of which the results of this study may need to be taken into consideration and, perhaps, extended. The first group includes various generalizations of the above spinor models (see, e.g., [39, 40]). We believe that similar NI can exist for them. Indeed, as was demonstrated in Section 7.2 and argued above in this section, it is the spinor character of the model rather than the specific form of nonlinearity that enables the occurrence of the NI.

The second group includes the Zakharov equations, describing interaction of short and long waves and consisting of an NLS coupled to the hyperbolic nonlinear wave equation [41]. It is the dispersion relation of this latter equation, which for high wavenumbers coincides with (5), which may potentially enable an NI similar to those considered in this work. In fact, an indication of a possible NI in simulations of the Zakharov equations by an SSM is reported in Fig. 10 of [12].

The possibility of occurrence of a NI similar to those considered in this work for the third group is the least certain and yet the most intriguing. Spinor-like, or coupled-mode, equations have been known to arise as small-amplitude reductions of the NLS with periodic potentials in one [42–44] and two [45, 46] spatial dimensions; see also summaries and references in, e.g., [22, 47]. The corresponding solitary wave is then called a gap soliton or Dirac soliton. Therefore, one may ask if either of the NI mechanisms studied here could affect the soliton stability observed in numerical simulations of those models. For example, in a recent study [48], it is reported that some analytically predicted weak physical instability could not be confirmed in numerical simulations by the SSM.[6] While this constitutes the opposite of NI (i.e., numerical stabilization), yet understanding of an

---

[6]Furthermore, [48] reports that the numerically observed stability properties of the gap soliton depend on the length L of the computational domain, which resembles our results reported in Figs. 8, 9, 11.

interplay between factors behind a *weak* physical instability and its numerical stabilization would need to rely on the linearization of the equations in a certain band of wavenumbers, just as we did in Sections 5 and 6. Moreover, note that in the presence of a periodic potential, the dispersion relation $\omega = \omega(k)$ will have inflection points (where $d^2\omega/\Delta k^2 = 0$, and hence (5) holds locally), which is one of the necessary ingredients of the "noise floor" NI; see the derivation of (39).

Line solitons of the coupled-mode equations in two spatial dimensions that arise as small-amplitude reductions of the corresponding NLS were shown [22] to be unstable with respect to transverse perturbations. Therefore, a NI, if present, may not have the time to manifest itself over the finite lifetime of those coherent structures. However, it is known (see, e.g., [49]) that *finite-amplitude* line solitons may acquire stability against transverse perturbations. Thus, in modeling such gap or Dirac solitons, an understanding and hence avoidance of NI become essential.

Acknowledgement

Appendix A: Code of 2nd-order SSM for Gross–Neveu soliton

```
1   clear all;
2   % —— Simulation parameters:
3   L = 40*pi;  N = 2^12;  dx = L/N;  x = [ -L/2 :dx: L/2-dx ];
4   dk = 2*pi/L;  k = [ 0 : N/2-1   -N/2 : -1 ]*dk;
5   dt = dx/2;  tmax = 1500;  tplot = 50;
6   % —— Initial conditions:
7   Omega = 0.35;  beta = sqrt( 1 - Omega^2 );  mu = (1 - Omega)/(1 + Omega);
8   u0 =    sqrt(2*(1 - Omega))./( (1 - mu*tanh(beta*x).^2).*cosh(beta*x) );
9   v0 = 1i*u0.*sqrt(mu).*tanh(beta*x);
10  u = u0 + 10^(-12)*randn(size(x));  v = v0 + 10^(-12)*randn(size(x));
11  % —— Auxiliary parameters to be used at each step in the loop:
12  idt = 1i*dt;  ckdt = cos(k*dt);  mi_skdt = -1i*sin(k*dt);
13  ckdto2 = cos(k*dt/2);  mi_skdto2 = -1i*sin(k*dt/2);
14  % —— Main calculation:
15    for nn = 1 : round(tmax/dt)
16        fftu = fft(u);  fftv = fft(v);
17        if nn == 1
18            u = ifft( ckdto2.*fftu + mi_skdto2.*fftv );
19            v = ifft( ckdto2.*fftv + mi_skdto2.*fftu );
20        else
21            u = ifft( ckdt.*fftu + mi_skdt.*fftv );
22            v = ifft( ckdt.*fftv + mi_skdt.*fftu );
23        end
24        expaux = exp( idt*( (abs(u).^2-abs(v).^2) - 1) );
25        u = u.*expaux;  v = v./expaux;
```

```
26        if  nn == round(tmax/dt)
27            u = ifft( ckdto2.*fftu + mi_skdto2.*fftv );
28            v = ifft( ckdto2.*fftv + mi_skdto2.*fftu );
29        end
30      % ---- Plot the results:
31      if  rem(nn, round(tplot/dt)) == 0
32            figure(123);
33            subplot(211); plot(x, abs(u), 'b', x, abs(v), 'r');
34            xlabel('x'); ylabel('{|u|, |v|}');
35            subplot(212); plot(k, log10(abs(fftu)), 'b', k, log10(abs(fftv)), 'r
                ');
36            xlabel('k, wavenumber'); ylabel('log_{10}(|F[u, v](k)|)');
37            title(['t=', num2str(dt*nn)], 'fontsize', 13); pause(0.3)
38        end
39   end
```

Appendix B: Some properties of growing modes near $k_{n\pi}$, and weak fragility of solitons with $\Omega > 0.6$

We will briefly list only those numerically observed properties of the (sub)linearly increasing modes near $k_{n\pi}$ that will help us explain the difficulty in understanding the origin of these modes.

1. The amplitude of these $k_{n\pi}$-peaks does *not* depend on the magnitude of the white noise added to the initial soliton; in Section 3 that amount was $\sim 10^{-12}$.

2. At sufficiently long times, the spectrum of the peaks near $k_{n\pi}$ resembles that of the soliton.

3. The peaks' amplitude does not show any consistent dependence on Δt (as long as $\Delta t > \Delta x$, so that the peaks can appear) or the length L of the computational domain.

4. The existence of these peaks is not affected by the presence of absorbing boundaries.

Property 1, along with the fact that in many simulations the peaks' amplitude grows linearly in time, suggests that the corresponding Fourier modes, $\widehat{p}(k)$, satisfy an equation of the form

$$\left(\partial_t + \widehat{\mathcal{L}}_p \right) \widehat{p} = \widehat{S}, \tag{B.1}$$

where $\widehat{\mathcal{L}}_p$ is some linear operator and $\widehat{S}$ is a source term *that is independent of $\widehat{p}$.* In other words, these modes grow due to a resonant excitation by some external force rather than due to a linear or nonlinear instability. Property 2 suggests that this external force is provided by the background soliton. In principle, such resonantly growing modes are well known in many contexts; e.g., in studies of optical solitons they occur due to higher-order dispersion or periodic amplification (see, e.g., [50, 51] and references therein). However, the key difference between the latter situations and the one with $k_{n\pi}$-peaks is that the resonant modes growing due to higher-order dispersion or periodic amplification occurred at those wavenumbers where the soliton's spectrum was small but nonzero. In contrast, the $k_{n\pi}$-peaks occur so far in the Fourier domain from the soliton that the

35

soliton's spectrum is zero at $|k| = k_{n\pi}$ to the machine round-off error. Thus, the origin of the source term in (B.1) remains unclear.

As an aside, let us note that the "Δt-part" of Property 3 implies that the source term in (B.1) is not provided by the discretization error of the SSM; this is consistent with the fact that such an error has most of its energy in the same modes as the soliton, i.e., near $k = 0$. Finally, Property 4 and the "L"-part of Property 3 imply that the field corresponding to the $k_{n\pi}$-peaks is localized in the x-domain, and thus so must be the source term in (B.1). This agrees with our earlier statement that this term is probably engendered by the soliton, but, unfortunately, this does not help one resolve the conundrum described in the previous paragraph.

We will now make a somewhat unexpected, but logical connection to the weak fragility of solitons with sufficiently high values of Ω, which up to now have been reported in the literature as non-fragile. Simulations reported in Section 3.1 illustrated our general observation that if the soliton is fragile, then exponentially growing modes will appear around $k_{n\pi}$-peaks whenever $\Delta t > \Delta x$. One can conjecture that the converse statement may also be true, namely: If one detects such modes around $k_{n\pi}$-peaks, then the soliton must be (weakly) fragile, even though it has not yet exhibited any fragile behavior for the same simulation time. In other words, can a purely numerical instability signal the occurrence of a physical one?

In Fig. 13 we demonstrate that this is indeed the case. In panel (a) we show a close-up on the vicinity of the k_π-peak for the $\Omega = 0.75$-soliton at $t = 15,000$, where exponentially growing "spikes" near the wider k_π-peak are clearly discernible. For the same t, there is no trace of fragile behavior of this numerical solution in either the Fourier or x-domains (panels (b) and (c)). However, at a much greater time, $t = 40,000$ a small "spike" becomes visible within the soliton's own spectrum (around $k = 5$); see Fig. 13(b). Finally, Fig. 13(d) shows that one can detect the exponentially growing modes around the k_π-peaks much earlier than similarly growing modes around the soliton.

We also verified that qualitatively the same behavior occurs for the $\Omega = 0.80$-soliton, except that it requires a factor of 3–4 longer simulation times to notice signs of fragile behavior: $t \sim 16,000$ for the numerical artefacts near k_π and $t \sim 70,000$ for the "spikes" around $|k| \approx 5$, which signal a commencement of the truly (albeit weakly) fragile behavior of the soliton. We remind the reader that a reason behind the emergence of the exponentially growing spectral "spikes", which are likely related to the fragility of the soliton, is not understood at present.

Two clarifications regarding the above result are in order. First, the reason that exponentially growing modes are observed sooner around the k_π-peak is that the "noise floor", from which these modes arise, is several orders of magnitude closer to the k_π-peak than to the soliton's spectral maximum. Thus, it takes less time for such modes to become visible relative to the k_π-peak than relative to the soliton. Second, the reason why the emergence of the exponential instability is significantly delayed from the start of the simulations (see Fig. 13(d)) was explained in [38, 52]. In brief, this delay is related to the fact that both (i) the overlap of the actual unstable mode with any one Fourier harmonic and (ii) the instability growth rate, are small.
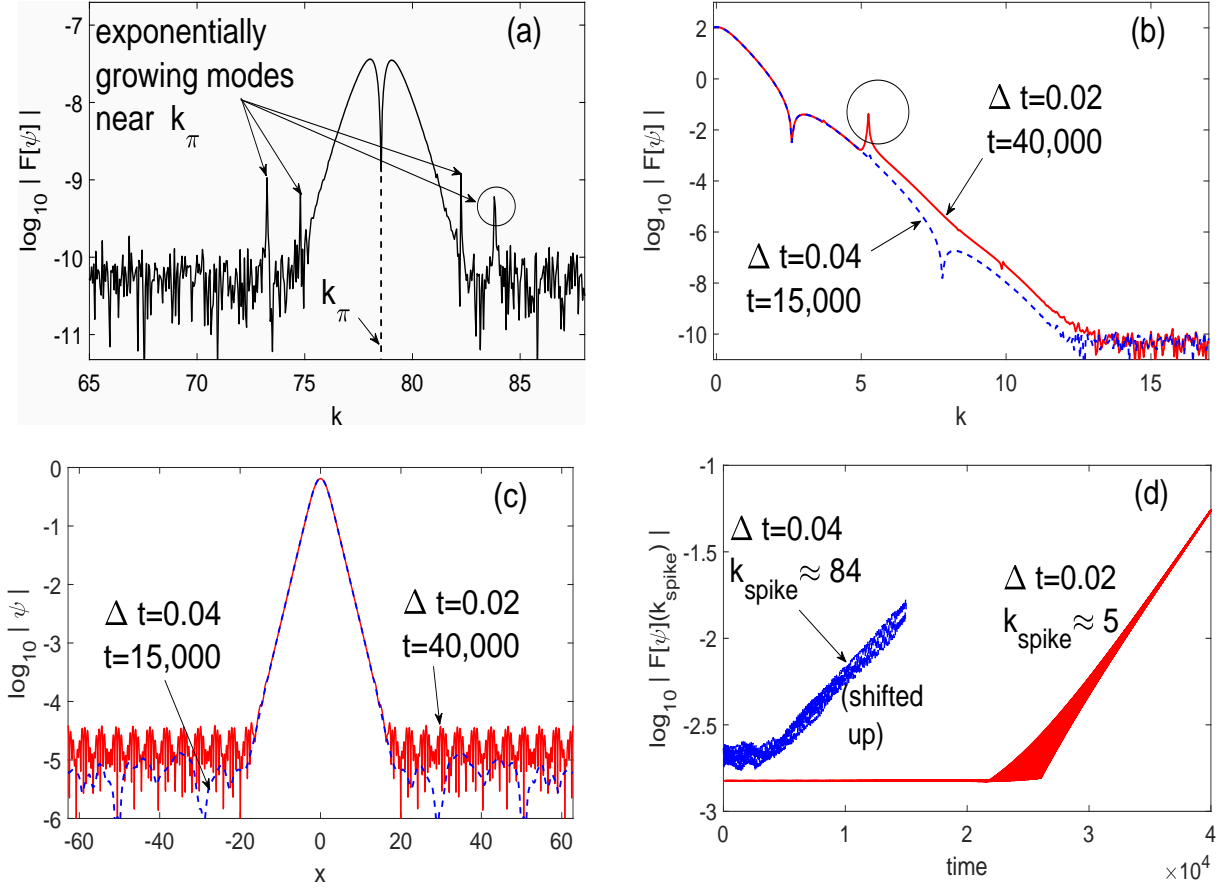
Figure 13: Ultra-long-time simulations of $\Omega = 0.75$-soliton (non-fragile). Simulation parameters are: $L = 40\pi$, $N = 2^{12}$ ($\Delta x = \Delta t_{\text{thresh}} \approx 0.031$). Results for the ψ_2-component are similar to those for the ψ_1-component and hence are not shown. (a) Close-up on the vicinity of the k_π-peak for $\Delta t = 0.04 \approx 1.3\Delta x$ and $t = 15,000$. (b) Solitonic part of the spectrum of the numerical solution obtained at different times and with different Δt. The lines are indistinguishable for $k < 5$. (c) Logarithmic plot of the numerical solution in the x-domain. The two curves are indistinguishable for $|x| \lesssim 20$. (d) Evolution of the amplitudes of the "spikes" circled in panels (a) and (b). The left curve is shifted up by 7.2 units for better visibility.

Appendix C: Alternative form of Eqs. (31), and their qualitative analysis in x-space

Substitution of (32) and (33) into Eqs. (31) and taking complex conjugate of two of the four equations yields the following system:

$$\widehat{a}_{(+),t} = \tag{C.1a}$$

$$i\left(\Omega - \delta k^{(<0)}\right)\widehat{a}_{(+)} + i\,\mathcal{F}\left[\left[P_0\,a_{(+)} + (iP_2 + P_3)b_{(-)} + Q_3\,a^*_{(-)} + (Q_0 + Q_1)b^*_{(+)}\right]^{(<0)}\right],$$

$$\widehat{b}_{(-),t} = \tag{C.1b}$$

$$i\left(\Omega + \delta k^{(\geq 0)}\right)\widehat{b}_{(-)} + i\,\mathcal{F}\left[\left[(-iP_2 + P_3)a_{(+)} + P_0\,b_{(-)} + (Q_0 - Q_1)a^*_{(-)} + Q_3\,b^*_{(+)}\right]^{(\geq 0)}\right].$$

37

$$\widehat{a}^*_{(-),t} = \tag{C.1c}$$

$$-i\left(\Omega + \delta k^{(<0)}\right)\widehat{a}^*_{(-)} - i\left(\mathcal{F}\left[\left[(Q_3\, a^*_{(+)} + (Q_0 - Q_1)b^*_{(-)} + P_0\, a_{(-)} + (-iP_2 + P_3)b_{(+)}\right]^{(<0)}\right]\right)^*,$$

$$\widehat{b}^*_{(+),t} = \tag{C.1d}$$

$$-i\left(\Omega - \delta k^{(\geq 0)}\right)\widehat{b}^*_{(+)} - i\left(\mathcal{F}\left[\left[(Q_0 + Q_1)a^*_{(+)} + Q_3\, b^*_{(-)} + (iP_2 + P_3)a_{(-)} + P_0\, b_{(+)}\right]^{(\geq 0)}\right]\right)^*.$$

Here we have also used that $P_1 = Q_2 = 0$ from (11).

Taking the inverse Fourier transform of these equations and seeking the solution in the form $\{a_{(+)}, b_{(-)}, a^*_{(-)}, b^*_{(+)}\} = \exp[i\Lambda t]\{\grave{a}_{(+)}, \grave{b}_{(-)}, \grave{a}^*_{(-)}, \grave{b}^*_{(+)}\}$, where $\grave{a}_{(+)}$ etc. do not depend on t, one obtains similarly to (20):

$$\grave{a}_{(+),x} + i(\Lambda - \Omega)\grave{a}_{(+)} = i\left[P_0\,\grave{a}_{(+)} + (iP_2 + P_3)\grave{b}_{(-)} + Q_3\,\grave{a}^*_{(-)} + (Q_0 + Q_1)\grave{b}^*_{(+)}\right]^{(<0)}, \tag{C.2a}$$

$$\grave{b}_{(-),x} - i(\Lambda - \Omega)\grave{b}_{(-)} = -i\left[(-iP_2 + P_3)\grave{a}_{(+)} + P_0\,\grave{b}_{(-)} + (Q_0 - Q_1)\grave{a}^*_{(-)} + Q_3\,\grave{b}^*_{(+)}\right]^{(\geq 0)}, \tag{C.2b}$$

$$\grave{a}^*_{(-),x} + i(\Lambda + \Omega)\grave{a}^*_{(-)} = -i\left[(Q_3^*\,\grave{a}_{(+)} + (Q_0 - Q_1)^*\grave{b}_{(-)} + P_0^*\,\grave{a}^*_{(-)} + (-iP_2 + P_3)^*\grave{b}^*_{(+)}\right]^{(<0)}, \tag{C.2c}$$

$$\grave{b}^*_{(+),x} - i(\Lambda + \Omega)\grave{b}^*_{(+)} = i\left[(Q_0 + Q_1)^*\grave{a}_{(+)} + Q_3^*\,\grave{b}_{(-)} + (iP_2 + P_3)^*\grave{a}^*_{(-)} + P_0^*\,\grave{b}^*_{(+)}\right]^{(\geq 0)}. \tag{C.2d}$$

This eigenvalue problem is to be solved with the periodic boundary conditions

$$\grave{a}_{(\pm)}(-L/2) = \grave{a}_{(\pm)}(L/2), \qquad \grave{b}_{(\pm)}(-L/2) = \grave{b}_{(\pm)}(L/2), \tag{C.3}$$

which are imposed by the discrete Fourier transform. Such an eigenvalue problem is considerably more complicated than an eigenvalue problem that follows from (27) and defines the physical stability of the Gross–Neveu solitons, because the "potential" terms on the r.h.s. are non-local, unlike those in (27). Nonetheless, it is still possible to draw two conclusions from (C.3).

First, since the eigenvalue problem (C.2), (C.3) is different than that which defines the physical stability of the soliton, the stability (or instability) of the harmonics at the edges of the computational spectrum is in no way related to the stability of the soliton. This distinguishes the former numerical (in)stability from that considered at the end of Section 4.

Second, (C.2) allows one to qualitatively explain the feature seen in Fig. 7, where the spectral peaks are separated by approximately 2Ω. The reasoning behind this goes as follows. While the integro-differential system (C.2) cannot be solved analytically,[7] it can be solved approximately if one assumes that $\widehat{a}_{(+)}$ etc. are much narrower (in the Fourier space) than $\widehat{P_0}$ etc., i.e.

$$\grave{a}_{(+)}(x) \simeq \grave{a}_{(+)}(0)\, e^{i\kappa_1 x}, \quad \grave{b}_{(-)}(x) \simeq \grave{b}_{(-)}(0)\, e^{i\kappa_2 x}, \quad \grave{a}^*_{(-)}(x) \simeq \grave{a}^*_{(-)}(0)\, e^{i\kappa_3 x}, \quad \grave{b}^*_{(+)}(x) \simeq \grave{b}^*_{(+)}(0)\, e^{i\kappa_4 x}, \tag{C.4}$$

for some $\kappa_{1,2,3,4}$. This approximation is rather inaccurate for Ω that are not sufficiently large (e.g., for $\Omega = 0.2$ and 0.35: see Fig. 7), but it is still self-consistent. Indeed, ansatz (C.4) implies that

$$\left[P_0\,\grave{a}_{(+)}\right]^{(<0)} \simeq \left[P_0\, e^{i\kappa_1 x}\right]^{(<0)}\grave{a}_{(+)}(0), \tag{C.5}$$

---

[7]Note that the differential system (27) for the physical stability of the soliton cannot be solved analytically, either, and it had to be solved numerically by the Evans function method in [21].

and similarly for the other terms on the r.h.s. of (C.2). Substitution of (C.5) into the r.h.s. of (C.2) and solving the remaining linear inhomogeneous differential system with the boundary condition (C.3) could allow one, in principle, to determine Λ.[8] The key thing to notice is that the coefficients of the inhomogeneous term *decay with* x:

$$\left[P_0\, e^{i\kappa_1 x}\right]^{(<0)} \sim 1/|x| \ll 1, \quad |x| \gg 1, \tag{C.6}$$

and similarly for the other coefficients. (This rather slow decay is due the discontinuity, owing to the "(<0)" superscript, of the integrand in the Fourier space.) Because of this strong inequality, it follows from (C.2) that far from the soliton approximation (C.4) is indeed valid. Then, $\kappa_{1,2,3,4}$ are found by substituting (C.4) into the l.h.s. of (C.2) and neglecting the r.h.s.:

$$\kappa_1 \approx \Omega - \Lambda, \quad \kappa_2 \approx -\Omega + \Lambda, \quad \kappa_3 \approx -\Omega - \Lambda, \quad \kappa_4 \approx \Omega + \Lambda, \tag{C.7a}$$

from which the statement at the beginning of this paragraph follows:

$$\kappa_1 - \kappa_3 \approx \kappa_4 - \kappa_2 \approx 2\Omega. \tag{C.7b}$$

Appendix D: Matrix blocks in (34c)

The $M \times M$ matrix blocks $\mathbb{C}_{1\,m}$, $m = 1, \ldots, 4$ are obtained from the respective four convolution-like terms in (C.1a). Similarly, the other blocks are obtained from the respective terms in (C.1b)–(C.1d). Here we will present a derivation of $\mathbb{C}_{11}$ and $\mathbb{C}_{12}$ and will state the results for the other $\mathbb{C}_{jm}$, which are derived analogously.

To obtain the form of $\mathbb{C}_{11}$, we substitute the first relation from (28) into the first $\mathcal{F}$-term in (C.1a) and use the definitions of discrete Fourier transform and its inverse (16) to obtain the following expression for the harmonic with wavenumber $k_{-j} = -j\Delta k$, where $1 \leq j \leq M$:

$$\mathcal{F}\left[P_0\, a_{(+)}\right]_{-j} = \sum_{m=-N/2}^{N/2-1} e^{-ik_{-j}x_m} \frac{1}{N} \sum_{n=-N/2}^{N/2-1} \widehat{P_0}_{\,n}\, e^{ik_n x_m} \frac{1}{N} \sum_{l=1}^{M} \widehat{a}_{(+)\,l}\, e^{-ik_l x_m} \tag{D.1}$$

$$= \frac{1}{N^2} \sum_{n=-N/2}^{N/2-1} \widehat{P_0}_{\,n} \sum_{l=1}^{M} \widehat{a}_{(+)\,l}\, \delta_{n,\,l-j} = \frac{1}{N} \sum_{l=1}^{M} \widehat{P_0}_{\,l-j}\, \widehat{a}_{(+)\,l};$$

in the last line, δ is the Kroneker symbol. Therefore,

$$\mathbb{C}_{11} = \begin{pmatrix} \widehat{P_0}_{\,0} & \widehat{P_0}_{\,1} & \cdots & \widehat{P_0}_{\,M-1} \\ \widehat{P_0}_{\,-1} & \widehat{P_0}_{\,0} & \cdots & \widehat{P_0}_{\,M-2} \\ \ddots & \ddots & \ddots & \ddots \\ \widehat{P_0}_{\,-(M-1)} & \widehat{P_0}_{\,-(M-2)} & \cdots & \widehat{P_0}_{\,0} \end{pmatrix}. \tag{D.2a}$$

This is a Toeplitz matrix, and half of the entries in (34c) will also be Toeplitz. Therefore, we introduce a notation:

$$\mathbb{C}_{11} \equiv \mathcal{T}\left[P_0, -(M-1), M-1\right], \tag{D.2b}$$

---

[8]For the aforementioned reason, for $\Omega \lesssim 0.35$, this approach leads to a much less accurate estimate of Λ, and is not simpler, than the straightforward approach described in Section 5; therefore we omit the details.

where: $\mathcal{T}$ stands for a Toeplitz matrix, the first argument indicates the function whose harmonics make up the entries of the matrix, and the third and fourth entries indicate the harmonic's indices of the lower-left and upper-right entries of the matrix, respectively. Note that the harmonic's index on the main diagonal of such a matrix is the average of the latter two indices.

Similarly, and denoting $iP_2 + P_3 \equiv P_{i23}$ for brevity, one has:

$$\mathcal{F}\left[P_{i23}\,b_{(-)}\right]_{-j} = \sum_{m=-N/2}^{N/2-1} e^{-ik_{-j}x_m} \frac{1}{N} \sum_{n=-N/2}^{N/2-1} \widehat{P_{i23}}_n \, e^{ik_n x_m} \frac{1}{N} e^{-i\Delta k x_m} \sum_{l=1}^{M} \widehat{b}_{(-)\,l} \, e^{ik_l x_m} \quad \text{(D.3)}$$

$$= \frac{1}{N} \sum_{l=1}^{M} \widehat{P_{i23}}_{\,1-l-j} \, \widehat{b}_{(-)\,l};$$

whence

$$\mathbb{C}_{12} = \begin{pmatrix} \widehat{P_{i23}}_{-1} & \widehat{P_{i23}}_{-2} & \cdots & \widehat{P_{i23}}_{-M} \\ \widehat{P_{i23}}_{-2} & \widehat{P_{i23}}_{-3} & \cdots & \widehat{P_{i23}}_{-M-1} \\ \ddots & \ddots & \ddots & \ddots \\ \widehat{P_{i23}}_{-M} & \widehat{P_{i23}}_{-M-1} & \cdots & \widehat{P_{i23}}_{-2M+1} \end{pmatrix}. \quad \text{(D.4a)}$$

This is a Hankel (i.e. an "upside-down" Toeplitz) matrix, and the remaining half of the entries in (34c) are also Hankel. Therefore, we introduce a notation:

$$\mathbb{C}_{12} \equiv \mathcal{H}\left[iP_2 + P_3,\, -1,\, -2M+1\right], \quad \text{(D.4b)}$$

where, similarly to (D.2b): $\mathcal{H}$ stands for a Hankel matrix, the first argument indicates the function whose harmonics make up the entries of the matrix, and the third and fourth entries indicate the harmonic's indices of the upper-left and lower-right entries of the matrix, respectively. Note that the harmonic's index on the main anti-diagonal of such a matrix is the average of the latter two indices.

Similarly, one has:

$$\mathbb{C}_{13} = \mathcal{H}\left[Q_3,\, -2,\, -2M\right], \qquad \mathbb{C}_{14} = \mathcal{T}\left[Q_0 + Q_1,\, -M,\, M-2\right]; \quad \text{(D.5a)}$$

$$\mathbb{C}_{21} = \mathcal{H}\left[-iP_2 + P_3,\, 1,\, 2M-1\right], \quad \mathbb{C}_{22} = \mathcal{T}\left[P_0,\, M-1,\, -(M-1)\right],$$
$$\mathbb{C}_{23} = \mathcal{T}\left[Q_0 - Q_1,\, M-2,\, -M\right], \quad \mathbb{C}_{24} = \mathcal{H}\left[Q_3,\, 0,\, 2M-2\right]; \quad \text{(D.5b)}$$

$$\mathbb{C}_{31} = -\mathcal{H}\left[Q_3^*,\, -2,\, -2M\right], \qquad\qquad \mathbb{C}_{32} = -\mathcal{T}\left[(Q_0 - Q_1)^*,\, -M,\, M-2\right],$$
$$\mathbb{C}_{33} = -\mathcal{T}\left[P_0^*,\, -(M-1),\, M-1\right], \quad \mathbb{C}_{34} = -\mathcal{H}\left[(-iP_2 + P_3)^*,\, -1,\, -2M+1\right]; \quad \text{(D.5c)}$$

$$\mathbb{C}_{41} = -\mathcal{T}\left[(Q_0 + Q_1)^*,\, M-2,\, -M\right], \quad \mathbb{C}_{42} = -\mathcal{H}\left[Q_3^*,\, 0,\, 2M-2\right],$$
$$\mathbb{C}_{43} = -\mathcal{H}\left[(iP_2 + P_3)^*,\, 1,\, 2M-1\right], \qquad \mathbb{C}_{44} = -\mathcal{T}\left[P_0^*,\, M-1,\, -(M-1)\right]. \quad \text{(D.5d)}$$

These matrix block can also be easily coded. For example, if `dftP0` and `dftPi23` denote the discrete Fourier spectra (16) with harmonics limited to $l \in [-2M,\, 2M]$ of P_0 and $(iP_2 + P_3)$, then the respective matrix blocks (D.2) and (D.4) can be programmed in Matlab as:

```
for j = 1 : M
   C_11(j, :) =   dftP0(2*M+1 - (j-1) : 2*M+1 - (j-1) + (M-1));
   C_12(j, :) = dftPi23(2*M - (j-1) :-1: 2*M - (j-1) - (M-1));
end
```

40

Appendix E: Explanation of why and how the spectral range of $\mathbf{\Phi}(L)$ depends on L

For the purpose of this explanation, it will suffice to replace the soliton with a box-like profile as follows. Since $\Psi_1(x)$ has a bell-like shape (even for small Ω when it is double-humped), we replace it by some constant for $x \in [-L_{\text{sol}}/2, L_{\text{sol}}/2]$. On the other hand, $i\Psi_2(x)$ changes sign at $x = 0$ (see Fig. 1), and therefore it needs to be replaced by a piecewise-constant profile on the same interval. Thus, we approximate:

$$\Psi_1(x) = \begin{cases} A, & x \in [-L_{\text{sol}}/2,\, L_{\text{sol}}/2] \\ 0, & |x| > L_{\text{sol}}/2 \end{cases} , \qquad \Psi_2(x) = \begin{cases} \pm iB, & x \in [0,\, \pm L_{\text{sol}}/2] \\ 0, & |x| > L_{\text{sol}}/2 \end{cases} , \qquad \text{(E.1a)}$$

for some $A, B, L_{\text{sol}} > 0$, with $L_{\text{sol}} \ll L$. Then the t-dependent matrix on the r.h.s. of (45) is replaced with:

$$\begin{pmatrix} \Psi_1^2 - \Psi_2^2 & (\Psi_1 + \Psi_2)^2 \\ (\Psi_1 - \Psi_2)^2 & \Psi_1^2 - \Psi_2^2 \end{pmatrix} = \begin{pmatrix} C & C\,e^{\pm i\phi} \\ C\,e^{\mp i\phi} & C \end{pmatrix}, \quad x \in [0,\, \pm L_{\text{sol}}/2] \qquad \text{(E.1b)}$$

and the zero matrix outside $[-L_{\text{sol}}/2,\, L_{\text{sol}}/2]$, where $C = A^2 + B^2$ and $\phi = 2\arctan(B/A)$.

Using the replacement (E.1b), we can now calculate $\mathbf{\Phi}(L)$ in (46) as

$$\mathbf{\Phi}(L) \equiv \mathbf{\Phi}_{L_{\text{sol}}}\, \mathbf{\Phi}_{\text{free}}, \qquad \mathbf{\Phi}_{L_{\text{sol}}} = \begin{pmatrix} \Phi_{11} & \Phi_{12} \\ -\Phi_{12} & \Phi_{11}^* \end{pmatrix}, \qquad \mathbf{\Phi}_{\text{free}} = e^{i\Omega(L - L_{\text{sol}})\boldsymbol{\sigma}_3} \qquad \text{(E.2)}$$

where the last matrix is obtained by solving the soliton-free part of (45) on an interval $t \in (L_{\text{sol}}/2,\, L - L_{\text{sol}}/2)$. The entries of $\mathbf{\Phi}_{L_{\text{sol}}}$ depend on A, B, and L_{sol} in a complicated way, but their explicit form is not needed for our purpose; we will only require the result, found by a tedious calculation, that $\Phi_{12} \in i\mathbb{R}$. The eigenvalues λ of $\mathbf{\Phi}(L)$ in (E.2) are found from the quadratic equation:

$$\lambda^2 - 2|\Phi_{11}| \cos\left[\Omega(L - L_{\text{sol}}) + \arg \Phi_{11}\right] \cdot \lambda + \left(|\Phi_{11}|^2 - |\Phi_{12}|^2\right) = 0. \qquad \text{(E.3)}$$

Since $\rho(\mathbf{\Phi}(L)) = |\lambda|$, one can see that it varies with L periodically, with the period being $2\pi/(2\Omega)$; this is verified by our numerical results, reported in Section 6. Moreover, as stated in (47),

$$\|\mathbf{\Phi}(L)\| = \rho\left(\mathbf{\Phi}(L)\,\mathbf{\Phi}^\dagger(L)\right)^{1/2} = \rho\left(\mathbf{\Phi}_{L_{\text{sol}}}\,\mathbf{\Phi}_{L_{\text{sol}}}^\dagger\right)^{1/2} = |\Phi_{11}| + |\Phi_{12}|, \qquad \text{(E.4)}$$

where $\dagger$ denotes Hermitian conjugation, and the last equation is found via a somewhat tedious but straightforward calculation. This result means that even when the "noise floor" does not grow *on average* over time, the amplitude of the "noise floor" harmonics can still increase by the factor $\|\mathbf{\Phi}(L)\|$ over a time $t = L$; however, it will decrease in one or more of subsequent time intervals of the same length.

Appendix F: Discussion of the instability related to the "noise floor" NI and seen in Fig. 9(b)

We will begin by presenting, in Fig. 14, numerical results for selected values of the length of the computational domain and for the parameters listed in Fig. 9. Observations from Fig. 14 can

be summarized as follows. The "noise floor" appears and disappears *differently* as one varies L. Namely, as L decreases from the upper end of the interval in question, the "noise floor" NI appears first at the greater wavenumbers and then (as L further decreases) occupies the larger part of the spectral domain. However, as L continues to decrease, the "noise floor" disappears at those higher wavenumbers where it initially appeared, its spectral support becomes localized and shifts towards smaller wavenumbers. As this occurs, the width of the unstable peak becomes much smaller than that of the soliton, and at the same time the rate of its shift towards lower wavenumbers decreases. This peak persists for significantly smaller δL than shown in Fig. 14(f) (we verified this up to $\delta L = -1.5$). However: (i) its growth rate decreases and (ii) is "climbs up" the soliton's "side". For this reason, it becomes impossible to accurately measure its growth rate (which in Fig. 9(b) is inferred from the height of the peak over the "noise floor"); this is why the corresponding data are *not* shown in that figure.
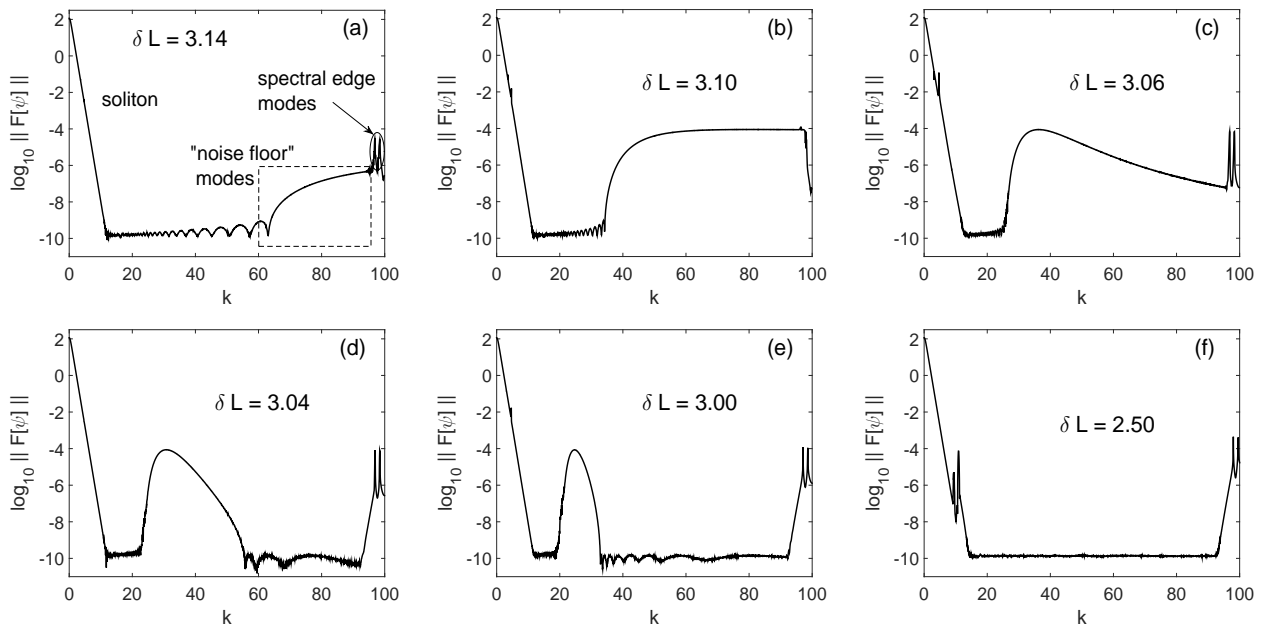

Figure 14: Numerical solution's spectrum (for $k \geq 0$) for the parameters listed in Fig. 9 and for the values of $\delta L \equiv L - 40\pi$ indicated in each panel. No "noise floor" (or related) NI was numerically observed for $\delta L \in [3.15, 4.2]$. On the other hand, the NI that "bifurcated" from the "noise floor" NI and is manifested by spectral peaks whose width decreases with δL, does persist for $\delta L < 2.50$; see text.

These observations suggest what modification to the analysis of Section 6 may account for the behavior illustrated in Fig. 14 and different from the predictions of that analysis. Note that the NI of the harmonics with highest wavnumbers follows the analytical predictions precisely; it is the behavior of the harmonics with *intermediate* wavenumbers (i.e., those much greater than the soliton's but still "not too large") that deviates from the analytical predictions. This indicates that one needs to account for the effect of rapidly oscillating terms $\widehat{a}^{(1)}$ and $\widehat{b}^{(1)}$, discarded in the derivation that lead from (36) to (39). A method to account for the effect of those terms is well known (see, e.g., [53], where it is applied to the Kapitza pendulum). Namely, one finds the first-order approximation for those terms from a counterpart of (24b) and substitutes the result (via

(37)) into (36), where those terms now produce a slowly-varying contribution when being averaged with the rapidly-oscillating coefficients. The magnitude of these terms will be proportional to $1/k$. That was low enough to not affect the (in)stability of the "noise floor" harmonics for $\Omega \lesssim 0.5$ (for which we did not notice such an effect), but apparently becomes significant for greater Ω where the growth rate itself becomes sufficiently low. Let us note that the new analysis would need to treat these unstable modes as spectrally localized 9as in Section 4 but not as in Section 6), as suggested by the numerical results shown in Fig. 14.

Thus, such an analysis is possible, but clearly quite cumbersome, and it is unclear what new insight it could contribute to the main results of this paper. For this reason, and also since it would matter only for ultra-long-time simulations, we did not carry it out.

References

[1] G. Strang, On the construction and comparison of difference schemes, SIAM J. Numer. Anal. 5 (1968) 506–517.

[2] M. Suzuki, Fractal decomposition of exponential operators with applications to many-body theories and Monte Carlo simulations, Phys. Lett. A 146 (1990) 319–323.

[3] H. Yoshida, Construction of higher order symplectic integrators, Phys. Lett. A 150 (1990) 262–268.

[4] M. Glassner, D. Yevick, B. Hermansson, High-order generalized propagation techniques, J. Opt. Soc. Am. B 8 (1991) 413–415.

[5] A.D. Bandrauk, H. Shen, Exponential split operator methods for solving coupled time-dependent Schrödinger equations, J. Chem. Phys. 99 (1993) 1185–1193.

[6] S.A. Chin, Multi-product splitting and Runge-Kutta-Nyström integrators, Celest. Mech. Dyn. Astr. 106 (2010) 391–406.

[7] R.H. Hardin, F.D. Tappert, Applications of the split-step Fourier method to the numerical soltion of nonlinear and variable coefficient wave equations, SIAM Review (Chronicle) 15 (1973) 423.

[8] T. Taha, M. Ablowitz, Analytical and numerical aspects of certain nonlinear evolution equations. II. Numerical, Nonlinear Schrodinger equation, J. Comput. Phys. 55 (1984) 203–230.

[9] W. Bao, H. Wang, An efficient and spectrally accurate numerical method for computing dynamics of rotating Bose–Einstein condensates, J. Comput. Phys. 217 (2006) 612–626.

[10] C.Z. Cheng, G. Knorr, The integration of the Vlasov equation in configuration space, J. Comput. Phys. 22 (1976) 330–351.

[11] J. de Frutos, J.M. Sanz-Serna, Split-step spectral schemes for nonlinear Dirac systems, J. Comput. Phys. 83 (1989) 407–423.

[12] W. Bao, F. Sun, G.W. Wei, Numerical methods for the generalized Zakharov system, J. Comput. Phys. 190 (2003) 201–228.

[13] S. Jin, P.A. Markowich, C. Zheng, Numerical simulation of a generalized Zakharov system, J. Comput. Phys. 201 (2004) 376–395.

[14] J.A.C. Weideman, B.M. Herbst, Split-step methods for the solution of the nonlinear Schrödinger equation, SIAM J. Numer. Anal. 23 (1986) 485–507.

[15] F. Matera, A. Mecozzi, M. Romagnoli, M. Settembre, Sideband instability induced by periodic power variation in long-distance fiber links, Opt. Lett. 18 (1993) 1499–1501.

[16] C. Francia, Constant step-size analysis in numerical simulation for correct four-wave-mixing power evaluation in optical fiber transmission systems, IEEE Photon. Technol. Lett. 11 (1999) 69–71.

[17] L. Gauckler, C. Lubich, Splitting integrators for nonlinear Schrödinger equations over long times, Found. Comput. Math. 10 (2010) 275–302.

[18] E. Faou, B. Grébert, E. Paturel, Birkhoff normal form for splitting methods applied to semi-linear Hamiltonian PDEs. Part I. Finite-dimensional discretization, Numer. Math. 114 (2010) 429–458.

[19] T.I. Lakoba, Instability analysis of the split-step Fourier method on the background of a soliton of the nonlinear Schrödinger equation, Numer. Methods Partial Differ. Equ. 28 (2012) 641–669.

[20] T.I. Lakoba, Instability of the split-step method for a signal with nonzero central frequency, J. Opt. Soc. Am. B 30 (2013) 3260–3271.

[21] G. Berkolaiko, A. Comech, On spectral stability of solitary waves of nonlinear Dirac equation in 1D, Math. Model. Nat. Phenom. 7 (2012) 13–31.

[22] D. Pelinovsky, Y. Shimabukuro, Transverse instability of line solitary waves in massive Dirac equations, J. Nonlinear Sci 26 (2016) 365–403.

[23] S. Shao, N.R. Quintero, F.G. Mertens, F. Cooper, A. Khare, A. Saxena, Stability of solitary waves in the nonlinear Dirac equation with arbitrary nonlinearity, Phys. Rev. E 90 (2014) 032915.

[24] J. Cuevas-Maraver, P.G. Kevrekidis, A. Saxena, F. Cooper, F.G. Mertens, Solitary waves in the nonlinear Dirac equation at the continuum limit: Stability and dynamics, In: Ord. Part. Diff. Eqs., (Nova Science, Boca Raton), Chap. 4.

[25] T.I. Lakoba, Numerical study of solitary wave stability in cubic nonlinear Dirac equations in 1D, Phys. Lett. A 382 (2018) 300–308.

[26] S.Y. Lee, T.K. Kuo, A. Gavrielides, Exact localized solutions of two-dimensional field theories of massive fermions with Fermi interactions, Phys. Rev. D 12 (1975) 2249–2253.

[27] A. Alvarez, B. Carreras, Interaction dynamics for the solitary waves of a nonlinear Dirac model, Phys. Lett. A 86 (1981) 327–332.

[28] G.W. Stewart, Introduction to Matrix Computations, (Academic, New York, 1973); Secs. 6.2 and 6.6.

[29] S.J. Orfanidis, R. Wang, Soliton solutions of the Massive Thirring model, Phys. Lett. B 57 (1975) 281–283.

[30] S.-J. Chang, S.D. Ellis, B.W. Lee, Chiral confinement: An exact solution of the massive Thirring model, Phys. Rev. D 12 (1975) 3572–3582.

[31] D.J. Kaup, A.C. Newell, On the Coleman correspondence and the solution of the Massive Thirring model, Lett. Nuovo Cimento 20 (1977) 325–331.

[32] E.A. Kuznetsov, A.V. Mikhailov, On the complete integrability of the two-dimensional classical Thirring model, Theor. Math. Phys. 30 (1977) 193–200.

[33] D.J. Kaup, T.I. Lakoba, The squared eigenfunctions of the massive Thirring model in laboratory coordinates, J. Math. Phys. 37 (1996) 308–323.

[34] H.G. Winful, Pulse compression in optical fiber fiters, Appl. Phys. Lett. 46 (1985) 527–529.

[35] I.V. Barashenkov, D.E. Pelinovsky, E.V. Zemlyanaya, Vibrations and Oscillatory Instabilities of Gap Solitons, Phys. Rev. Lett. 80 (1998) 5117–5120.

[36] S.M. Cox, P.C. Matthews, Exponential time differencing for stiff systems, J. Comput. Phys. 176 (2002) 430–455.

[37] F. de la Hoz, F. Vadillo, An integrating factor for nonlinear Dirac equations, Comput. Phys. Commun. 181 (2010) 1195–1203.

[38] T.I. Lakoba, Instability of the finite-difference split-step method applied to the nonlinear Schrödinger equation. II. moving soliton, Numer. Methods Partial Differ. Equ. 32 (2016) 1024–1040.

[39] A. Khare, F. Cooper, A. Saxena, Approximate analytic solutions to coupled nonlinear Dirac equations, Phys. Lett. A 381 (2017) 1081–1086.

[40] N.V. Alexeeva, I.V. Barashenkov, A. Saxena, Spinor solitons and their PT-symmetric offspring, Ann. Phys. 403 (2019) 198–223.

[41] V.E. Zakharov, Collapse of Langmuir waves, Sov. Phys. JETP 35 (1972) 908–914.

[42] O. Zobay, S. Pötting, P. Meystre, E.M. Wright, Creation of gap solitons in Bose–Einstein condensates, Phys. Rev. A 59 (1999) 643–648.

[43] P.J.Y. Louis, E.A. Ostrovskaya, C.M. Savage, Y.S. Kivshar, Bose–Einstein condensates in optical lattices: Band-gap structure and solitons, Phys. Rev. A 67 (2003) 013602.

[44] D.E. Pelinovsky, A.A. Sukhorukov, Y.S. Kivshar, Bifurcations and stability of gap solitons in periodic potentials, Phys. Rev. E 70 (2004) 036618.

[45] L.H. Haddad, L.D. Carr, The nonlinear Dirac equation in Bose–Einstein condensates: Foundation and symmetries, Physica D 238 (2009) 1413–1421.

[46] M.J. Ablowitz, S.D. Nixon, Y. Zhu, Conical diffraction in honeycomb lattices, Phys. Rev. A 79 (2009) 053830.

[47] G. Hwang, T.R. Akylas, J. Yang, Gap solitons and their linear stability in one-dimensional periodic media, Physica D 240 (2011) 1055–1068.

[48] P.P. Kizin, D.A. Zezyulin, G.L. Alfimov, Oscillatory instabilities of gap solitons in a repulsive Bose–Einstein condensate, Physica D 337 (2016) 58–66.

[49] J. Yang, D. Gallardo, A. Miller, Z. Chen, Elimination of transverse instability in stripe solitons by one-dimensional lattices, Opt. Lett. 37 (2012) 1571–1573.

[50] J.N. Elgin, Perturbations of optical solitons, Phys. Rev. A 47 (1993) 4331–4341.

[51] N. Akhmediev, M. Karlsson, Cherenkov radiation emitted by solitons in optical fibers, Phys. Rev. A 51 (1995) 2602–2607.

[52] T.I. Lakoba, Instability of the finite-difference split-step method applied to the nonlinear Schrödinger equation. III. external potential and oscillating pulse solutions, Numer. Methods Partial Differ. Equ. 33 (2016) 633–650.

[53] L.D. Landau, E.M. Lifshitz, Mechanics, 2nd Ed., (Pergamon, Oxford, 1969); Sec. 30.